Research Paper

GEOSPHERE

GEOSPHERE

https://doi.org/10.1130/GES02772.1

14 figures; 1 set of supplemental files

CORRESPONDENCE: clsitar5@gmail.com

CITATION: Sitar, M.C., Singleton, J.S., Rahl, J.M., Caine, J.S., King, J., Kylander-Clark, A., and O'Sullivan, P., 2025, Structural analysis of brittle-plastic shear zones in the Sangre de Cristo Range, southern Colorado: USA: Superposition of Rio Grande rift extension on Laramide contraction: Geosphere, https://doi.org/10.1130/GES02772.1.

Science Editor: David E. Fastovsky
Associate Editor: Jason W. Ricketts

Received 10 March 2024
Revision received 7 September 2024
Accepted 19 February 2025

Published online 25 March 2025

Structural analysis of brittle-plastic shear zones in the Sangre de Cristo Range, southern Colorado, USA: Superposition of Rio Grande rift extension on Laramide contraction

Michael C. Sitar[1], John S. Singleton[1], Jeffrey M. Rahl[2], Jonathan Saul Caine[3], Jacob King[1], Andrew Kylander-Clark[4], and Paul O'Sullivan[5]

[1]Department of Geosciences, Colorado State University, Fort Collins, Colorado 80523, USA
[2]Department of Earth and Environmental Geoscience, Washington and Lee University, 204 West Washington Street, Lexington, Virginia 24450, USA
[3]U.S. Geological Survey, Geology, Geophysics, and Geochemistry Science Center, Denver, Colorado 80225, USA
[4]Department of Earth Science, University of California, 1006 Web Hall, Santa Barbara, California 93106, USA
[5]GeoSep Services, 1521 Pine Cone Road, Moscow, Idaho 83843, USA

ABSTRACT

The Sangre de Cristo Range in southern Colorado exposes some of the deepest Cenozoic structural levels in the Rocky Mountain region, including mylonitic shear zones associated with both the Laramide orogeny and Rio Grande rift. We investigated the relation between Laramide contraction and Rio Grande rift extension with detailed geologic mapping, kinematic analysis, and geochronometry in a 50 km² area centered on the Independence Mine shear zone (IMSZ). The 15–100-m-thick IMSZ is one of several shallowly to moderately (~45° ± 20°) W-SW–dipping brittle-plastic shear zones along the western flank of the range. These shear zones display microstructural evidence of initiation as top-NE contractional mylonite zones, consistent with regional Laramide kinematics, which have been pervasively overprinted by shear fabrics indicating top-SW extensional reactivation. Both top-NE and top-SW shear fabrics involve cataclasis and quartz dislocation creep, although top-SW shear is more commonly localized along phyllosilicate-lined shear bands. Shear zones are hosted predominately within Proterozoic gneiss, and contain abundant chlorite and white mica derived from alteration of hornblende and feldspar, which indicates that weakening driven by fluid reactions played an important role in localizing strain. Extensional overprinting appears to be most pervasive along more steeply dipping portions of shear zones and where secondary phyllosilicates form an interconnected weak phase, which suggests that reactivation was primarily controlled by geometry and rheological contrasts inherited from contraction. One top-SW shear zone adjacent to the IMSZ cuts a late Oligocene gabbro stock, and monazite grains synkinematic with top-SW shear in the IMSZ yielded late Oligocene to Early Miocene U-Th-Pb dates that correspond with initiation of the Rio Grande rift. Reactivation of weak reverse faults may represent an important structural control during initial extension in the middle crust, prior to slip along the high-angle Sangre de Cristo normal fault system.

M. Cole Sitar https://orcid.org/0000-0003-0688-1067

1. INTRODUCTION

Shear zones play fundamental roles in accommodating strain in the middle to lower crust. The rheological and kinematic evolution of shear zones near the brittle-plastic transition is particularly important, as peak crustal strength typically resides in this zone (e.g., Sibson, 1983; Kohlstedt et al., 1995; Behr and Platt, 2014). The brittle-plastic transition zone may control the state of stress throughout the crust, affect the distribution and mechanisms of deformation, and influence fault (brittle) and shear zone (plastic) reactivation. The degree to which the behavior of this brittle-plastic zone is influenced by structural inheritance is not well understood, but investigation of exhumed brittle-plastic shear zones that have undergone polyphase deformation may provide important insight into the processes governing the reactivation and evolution of superposed orogens.

The conditions under which brittle faults may be reactivated are well understood. Brittle faults that are not optimally oriented in a stress field (e.g., non-Andersonian; Anderson, 1905) may be reactivated given a sufficiently high fluid pressure (ρ_f) and/or a low coefficient of static friction (μ; Byerlee, 1978; Sibson, 1985). Several studies of presently active faults suggest that frictionally weak clay minerals found in gouge can facilitate slip along misoriented faults in the upper crust, but these minerals break down at greater depths (>6–9 km), and slip along non-Andersonian faults and shear zones near the brittle-plastic transition are consequently somewhat enigmatic (Carpenter et al., 2012; Behr and Platt, 2014). Foliated shear fabrics dominated by chlorite and/or muscovite may form frictionally weak zones in the lower part of the brittle crust (e.g., Collettini et al., 2019), and fluid-assisted plastic flow of phyllosilicates may contribute to a weak fault/shear zone rheology near the brittle-plastic transition (e.g., Bos and Spiers, 2002; Wallis et al., 2015). In addition to increasing ρ_f, fluids may play important roles in weakening rocks and facilitating fault/shear zone reactivation. For example, chlorite is relatively strong while dry but weakens substantially when wet (Collettini, 2011), and fluids can weaken common stronger silicate minerals such as quartz by infiltrating

and disrupting their crystalline structures (i.e., "hydrolytic weakening;" Griggs, 1967). Fluid-rock reactions can likewise produce weaker minerals, such as phyllosilicates, through alteration of stronger minerals, such as amphiboles and feldspars (i.e., "reaction weakening;" e.g., O'Hara, 1988; Yonkee et al., 2003).

The Independence Mine shear zone (IMSZ) is a SW-dipping brittle-plastic shear zone characterized by chlorite-rich mylonites and exposed along the western flank of the Sangre de Cristo Range in southern Colorado. Because the IMSZ and related shear zones have been exhumed from the brittle-plastic transition, they provide a useful analogue for how structures that are suboptimally oriented with respect to an Andersonian regime behave at depth. Previous mapping at a scale of 1:24,000 or smaller led to interpretation of the IMSZ as a thrust fault (Clement, 1952; Lindsey et al., 1986a), but the structure has not been studied in detail. IMSZ mylonites commonly display fabrics consistent with top-SW (normal-sense) displacement that are locally mixed with fabrics and kinematic indicators consistent with top-NE (reverse-sense) displacement. Regional ENE–directed crustal shortening occurred during the Late Cretaceous to early Paleogene Laramide orogeny, with subsequent SW-directed extension associated with the Rio Grande rift initiating in the late Oligocene and continuing through the present day (e.g., Lindsey, 2010). Known local Laramide thrust faults mostly dip shallowly to the SW, whereas local Rio Grande rift-associated normal faults dip moderately to steeply to the SW (e.g., Brister and Gries, 1994; Kluth and Schaftenaar, 1994). The dip of the IMSZ generally appears to be intermediate to the dip of local Laramide and Rio Grande faults, and contradictory kinematic fabrics within it suggest that it may have been active during both events. Here, we present detailed geologic mapping of the IMSZ and adjacent structures in addition to microstructural and geochronological analyses to evaluate controls on reactivation and how deformation has been accommodated in the middle crust during regional shortening and rifting events.

2. GEOLOGIC SETTING

The NNW–trending Sangre de Cristo Range in Colorado constitutes the northern end of the broader Sangre de Cristo Mountains, which extend south to Santa Fe, New Mexico, and comprise the southernmost part of the Rocky Mountains (e.g., Lindsey, 2010; Fig. 1). Rocks in the Sangre de Cristo Range record a complex deformational history spanning from the Paleoproterozoic to the present. Polydeformed Proterozoic basement rocks dominate the western flank of the range. These rocks include Paleoproterozoic amphibolite and quartzofeldspathic gneisses that typically exhibit steeply dipping, NW-striking fabrics and isoclinal folds associated with the amalgamation of the Yavapai province between 1.75 Ga and 1.71 Ga ("D_1," per Jones and Connelly, 2006). This deformation event was followed by regional emplacement of felsic intrusions prior to a deformation event that produced localized NE-SW–striking fabrics in the range that have been interpreted to represent the late stages of the Mazatzal orogeny ("D_2," Jones and Connelly, 2006). A subsequent tectonic lull extending into the Mesoproterozoic was broken by the emplacement of the coarse-grained A-type quartz monzonite of Music Pass at ca. 1.43 Ga (Jones and Connelly, 2006) and shortly thereafter by an additional, poorly understood deformational event that produced NE-SW–trending folds and subvertical mylonitic fabrics in both Paleoproterozoic and Mesoproterozoic units ("D_3," Jones and Connelly, 2006).

The area of the modern Sangre de Cristo Range is interpreted to have experienced relative tectonic quiescence through the early Paleozoic, and a succession of units, including the Ordovician Harding Formation and the Mississippian Leadville Limestone, were deposited in marine settings, followed by widespread exposure and karst development (Clement, 1952; Lindsey, 2010). Late Paleozoic rocks in the range record uplift and erosion of the Ancestral Rocky Mountains. During the Pennsylvanian–Permian, the contemporary Sangre de Cristo Range was located in the Central Colorado trough, a depositional basin bounded by the Uncompahgre uplift to the southwest and the Ancestral Front Range and Apishapa uplifts to the northeast (Lindsey et al., 1986c; Hoy and Ridgway, 2002; Sweet et al., 2021; Smith et al., 2023). The Pennsylvanian Minturn Formation and Pennsylvanian–Permian Sangre de Cristo Formation were deposited in the Central Colorado trough and are cumulatively >4 km thick. An upward-coarsening trend in these units provides evidence of the relatively rapid exhumation and beveling of the Uncompahgre uplift, with deposition of the Crestone Conglomerate Member of the Sangre de Cristo Formation recording unroofing of the crystalline basement of the Uncompahgre uplift (Lindsey et al., 1986c; Hoy and Ridgway, 2002). The upper Paleozoic units of the Sangre de Cristo Range also preserve several primary Ancestral Rocky Mountains structures (Hoy and Ridgway, 2002) that are rarely exposed elsewhere (Sweet and Soreghan, 2010). These structures are generally consistent with NE-SW shortening and include the NW-SE–trending Gibson Peak growth syncline within the Sangre de Cristo Formation to the northeast of the study area and the Sand Creek thrust system to the south of the study area (Fig. 1A; Hoy and Ridgway, 2002). The Gibson Peak syncline has been interpreted to record Pennsylvanian–Permian syndepositional shortening along the Crestone thrust (Figs. 1 and 2) at the northeastern margin of the Uncompahgre uplift, which suggests that some thrust faults that later accommodated Laramide shortening originated during the Ancestral Rocky Mountains orogeny (Hoy and Ridgway, 2002). Such reactivation appears to have been localized. The Crestone Conglomerate Member overlaps a steeply W-dipping reverse fault named the Little Sand Creek thrust, which indicates that this fault was involved in early–middle Ancestral Rocky Mountains shortening but was not reactivated during the Laramide orogeny (Hoy and Ridgway, 2002; Lindsey and Caine, 2024). Some researchers have interpreted the Sand Creek thrust system as being contiguous with the folded Deadman Creek thrust fault along the western flank of the range (e.g., Lindsey et al., 1986a; Lindsey and Caine, 2024). The northern end of the Deadman Creek thrust fault is adjacent to the southern end of the IMSZ (Figs. 1 and 2), and, like the IMSZ, the Deadman Creek thrust fault includes mylonites involving Proterozoic basement rocks (Weigel, 2014; Lindsey and Caine, 2024).

In the early to middle Mesozoic, the area of the Sangre de Cristo Range was likely the site of renewed deposition prior to the onset of the Laramide orogeny in the Late Cretaceous, which is recorded by the sedimentary record in the Raton basin east of the range (Lindsey, 1998; Cather, 2004; Bush et al., 2016). Surface uplift may have begun as early as 80 Ma but certainly before 70 Ma (Cather, 2004; Bush et al., 2016; Thacker et al., 2023). During the Laramide orogeny, the current southwestern flank of the Sangre de Cristo Range was located within the San Luis uplift, which has been interpreted as accommodating spatially variable, kilometer-scale shortening along W- to SW-dipping thrusts and reverse faults, such as the Deadman Creek thrust and the reactivated Crestone thrust (Tweto, 1975; Hoy and Ridgway, 2002; Lindsey, 2010). Laramide slip histories for these faults that do not involve Mesozoic units have been interpreted largely based on indirect evidence, although NE-vergent thrust faults along the eastern flank of the range locally involve Mesozoic strata and thus clearly record Laramide deformation (e.g., the Loco Hill thrust; Lindsey et al., 1983). The Sand Creek thrust, which may correlate with the Deadman Creek thrust fault and its associated mylonite zone, cuts the entire thickness of the Pennsylvanian–Permian section and is interpreted to cut other thrust faults (the Crestone and Marble Mountain thrust), which suggests that it likely records Laramide (post-Ancestral Rocky Mountains) slip as well (Lindsey and Caine, 2024). The IMSZ may have originated contemporaneously as the mid-crustal counterpart of a similarly oriented Laramide thrust/reverse fault. Based on the sedimentary record in the Raton basin, Laramide uplift continued into the early Eocene and was followed by a period of erosional beveling (Cather, 2004; Bush et al., 2016; Lindsey and Caine, 2024). Conodont alteration indices within Pennsylvanian units suggest peak Laramide burial temperatures of up

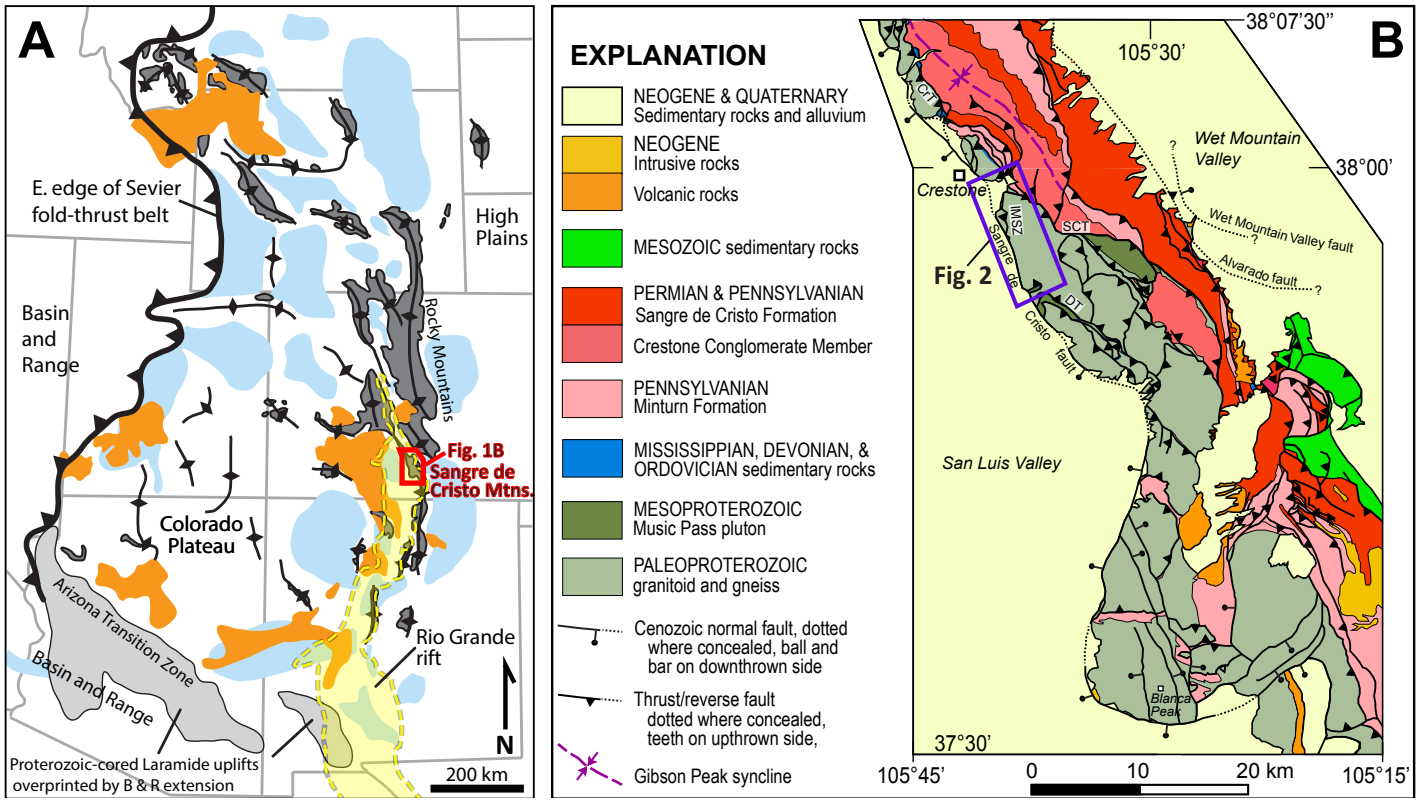

Figure 1. (A) Regional map of the Rocky Mountain region, USA, showing major Mesozoic–Cenozoic tectonic features (modified from Blakey and Ranney, 2018). Dark gray—basement-cored Laramide uplifts; blue—Laramide basins; lines with diamonds—trends of Laramide uplifts; orange—Cenozoic volcanic centers; yellow—Rio Grande rift basins. Red polygon outlines the Fig. 1B area. (B) Simplified geologic map of the Sangre de Cristo Range (modified from Johnson, 1969, Johnson et al., 1987, and Lindsey and Caine, 2024). B & R—Basin and Range; CrT—Crestone thrust; IMSZ—Independence Mine shear zone; SCT—Sand Creek thrust; DT—Deadman Creek thrust.

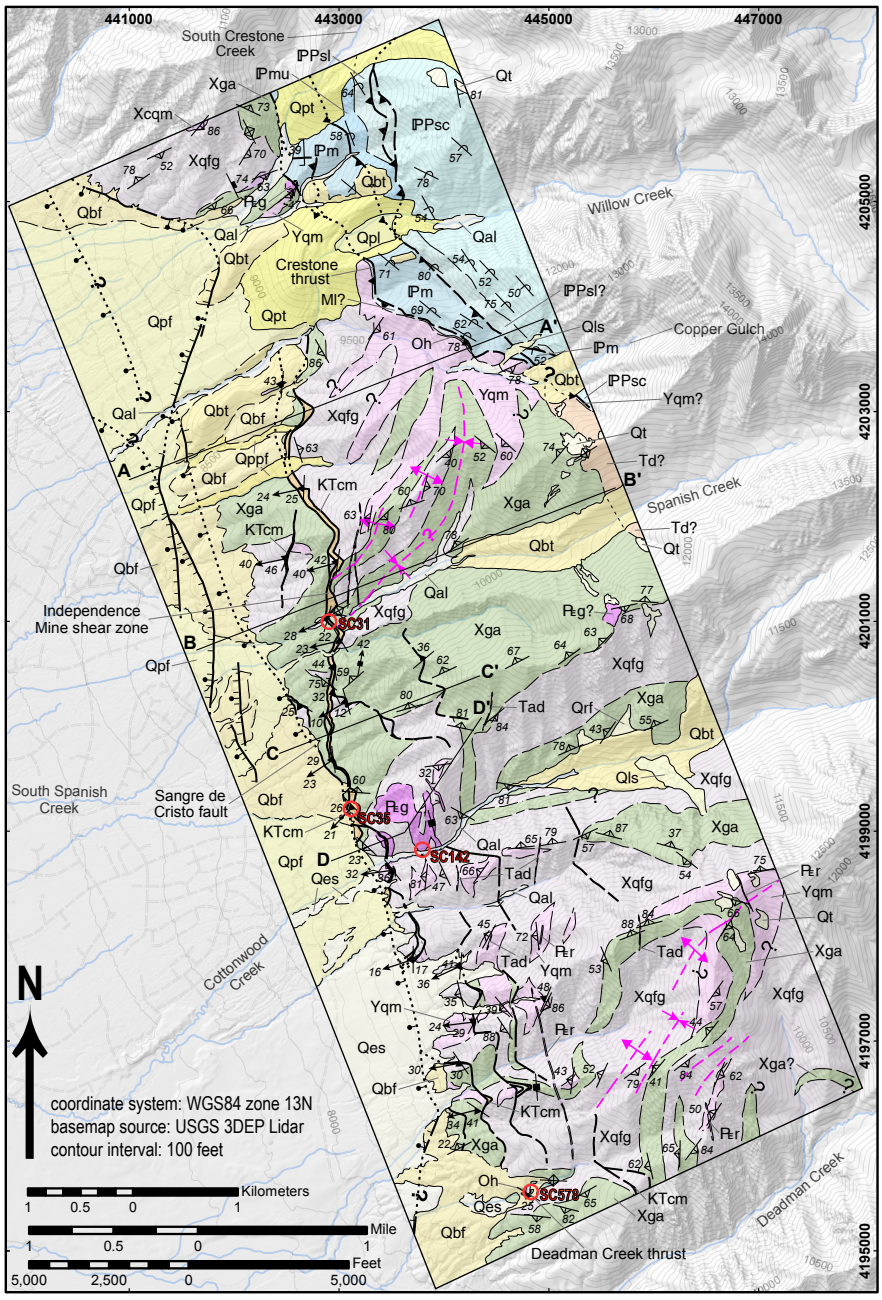

Geologic Map of the Western Flank of the Sangre de Cristo Range in the Vicinity of Crestone, CO

LIST OF MAP UNITS

ALLUVIAL, EOLIAN, & MASS WASTING

- Qal — Alluvium (Holocene)
- Qes — Eolian sand dunes (Holocene)
- Qt — Talus (Holocene)
- Qrf — Rockfall deposits (Holocene)
- Qls — Landslide deposits (Holocene)

GLACIAL & GLACIOFLUVIAL SEDIMENTS

- Qpf — Alluvial fan deposits of Pinedale glaciation (late Pleistocene)
- Qpl — Glacial lake deposits of Pinedale glaciation (late Pleistocene)
- Qpt — Till of Pinedale glaciation (late Pleistocene)
- Qppf — Pre-Pinedale alluvial fan deposits (middle-late Pleistocene)
- Qbf — Alluvial fan deposits of Bull Lake glaciation (late-middle Pleistocene)
- Qbt — Till of Bull Lake glaciation (late-middle Pleistocene)

MYLONITIC ROCKS

- KTcm — Chloritic mylonite (Early Miocene to late Oligocene and early Paleogene(?) to Late Cretaceous)

PALEOGENE VOLCANIC & INTRUSIVE

- Pɛr — Rhyolite dikes (Oligocene to late Eocene)
- Tad — Andesitic dikes (late Oligocene?)
- Pɛg — Gabbroic intrusions (late Oligocene)
- Td — Diorite intrusion (late Oligocene?)

PALEOZOIC SEDIMENTARY ROCKS

- ℙPsc — Crestone Conglomerate Member of Sangre de Cristo Formation (Permian-Pennsylvanian)
- ℙPsl — Informal lower member of Sangre de Cristo Formation (Permian-Pennsylvanian)
- ℙmu — Informal upper member of Minturn Formation (Pennsylvanian)
- ℙm — Minturn Formation, undivided (Pennsylvanian)
- Ml — Leadville Limestone (Mississippian)
- Oh — Harding Formation (Ordovician)

PROTEROZOIC INTRUSIVE

- Yqm — Quartz monzonite (Mesoproterozoic)
- Xcqm — Quartz monzonite of Crestone (Paleoproterozoic)

PROTEROZOIC GNEISS

- Xqfg — Quartzo-feldspathic gneiss (Paleoproterozoic)
- Xga — Gneissic amphibolite (Paleoproterozoic)

SIMPLIFIED SYMBOLOGY EXPLANATION

CONTACTS, FAULTS, & SHEAR ZONES

- Contact
- Contact, approximate
- Contact, questionable
- Contact, concealed
- Contact, concealed & questionable
- Brittle-plastic shear zone margin
- Normal fault
- Normal fault scarp
- Thrust/reverse fault

Bedding
Bedding, vertical
Bedding, overturned
Cleavage

Gneissic foliation
Gneissic foliation, vertical
Mylonitic foliation
Mylonitic lineation

Mineral lineation
Joint
Joint, vertical

Antiform axial trace
Synform axial trace
sample for U-Pb

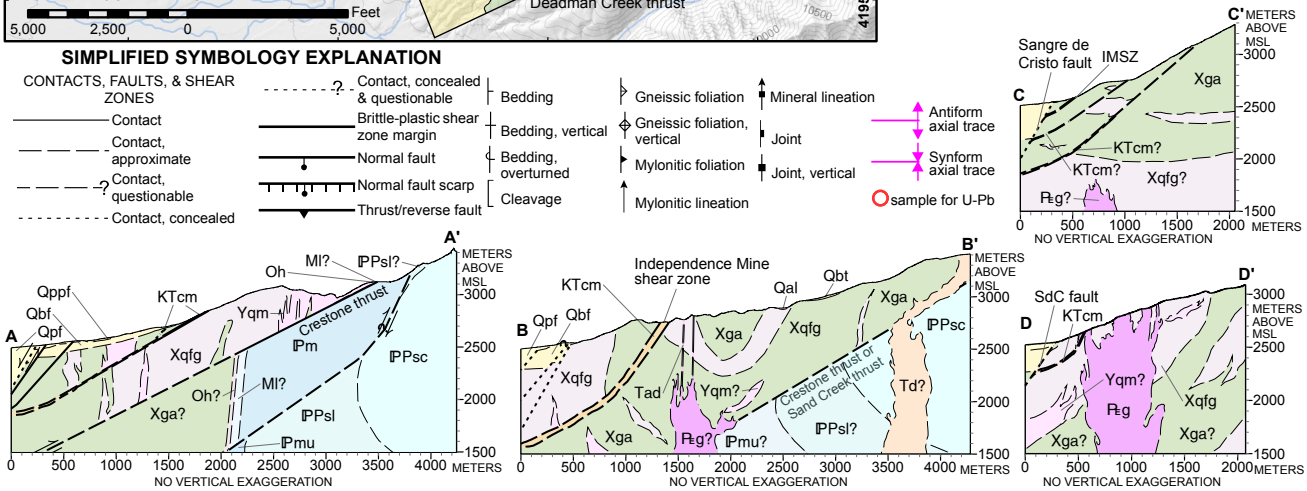

Figure 2. Simplified geologic map and cross sections of the study area based on new 1:10,000-scale mapping (File S1 provides a detailed 1:10,000-scale version of this map; see text footnote 1). IMSZ—Independence Mine shear zone; USGS—U.S. Geological Survey.

to ~300 °C along the western side of the Sangre de Cristo Range (Lindsey et al., 1986b), although some areas were locally heated to ~400–600 °C during Oligocene contact metamorphism (Malavarca et al., 2023).

Multiple lines of evidence indicate that extension and development of significant paleotopography associated with the Rio Grande rift began in the late Oligocene. Early Oligocene volcanic deposits were deposited across a relatively low-relief landscape, including the 28 Ma Fish Canyon Tuff, which erupted from the La Garita caldera to the west of the present Sangre de Cristo Range but also crops out along the western flank of the Wet Mountains east of the range (Steven and Lipman, 1975; McIntosh and Chapin, 2004). Further evidence from volcanic deposits (e.g., <26.8 Ma Hinsdale Formation basalt flows, which unconformably cover earlier Oligocene ash deposits; Lipman, 1975; Brister and Gries, 1994) suggests that extensional development of the San Luis basin north and west of Blanca Peak may have begun at ca. 27 Ma. $^{40}Ar/^{39}Ar$ dates for plutonic and volcanic rocks represented as clasts in basal syn-rift sediments indicate a slightly younger (ca. 25 Ma) initiation of rift-related extension in the Culebra embayment south of Blanca Peak (Wallace, 2004). In the San Juan volcanic field along the western margin of the rift, a switch to bimodal volcanism at ca. 26 Ma is interpreted to coincide with the inception of regional extension (Lipman et al., 1970; Lipman and McIntosh, 2011). Apatite low-temperature thermochronologic data from fission-track and (U-Th)/He analysis broadly suggest an onset of extensional unroofing between ca. 27 Ma to ca. 25 Ma (Lindsey et al., 1986b; Kelley et al., 1992; Ricketts et al., 2016). More recent thermochronologic studies indicate that exhumation rates rapidly increased in the Middle Miocene (Abbey and Niemi, 2020; Singleton et al., 2024), which is consistent with evidence of an increase in normal fault slip rates at ca. 15 Ma based on offset volcanic units in the Culebra Range (Miggins et al., 2002). Rio Grande rift extension along the eastern flank of the Sangre de Cristo Range was partially accommodated along the Alvarado fault, which likely originated as a Laramide thrust fault prior to normal-sense reactivation (Lindsey et al., 1983; Ghamedi et al., 2023). West-dipping faults in the San Luis Valley and near the western flank of the range have cumulatively accommodated ~9 km of normal-sense vertical separation, with the majority of this separation developed along the moderate- to high-angle (~60°) Sangre de Cristo fault system and geometrically similar buried normal faults (Kluth and Schaftenaar, 1994; Grauch et al., 2013). The strand of the Sangre de Cristo fault system along the topographic base of the range likely has <300 m of separation in most places (Watkins, 1996; Grauch et al., 2013), and a W-dipping fault nearly 7 km west of the range front in the San Luis Valley records the largest separation (Kluth and Schaftenaar, 1994; Grauch et al., 2013). The steep dips of the Sangre de Cristo fault system and overall low dips of basin strata (Kluth and Schaftenaar, 1994) suggest that the range has undergone little tilting. Relatively well-defined fault scarps in Quaternary sediments indicate that extension along the Sangre de Cristo fault system has continued into the Holocene (McCalpin, 1981; Ruleman and Brandt, 2021). Other higher- and lower-angle SW-dipping normal faults have been noted or proposed along the western flank of the range (Benson and Jones, 1996; Watkins, 1996; Hoey et al., 2006; Caine et al., 2013), but their significance in accommodating Rio Grande rift-related extension is unclear. The role played by preexisting thrust faults along the western flank of the range during Rio Grande rifting is likewise poorly understood, although some workers have interpreted rift-related reactivation of Laramide thrusts to the north (Fletcher et al., 2006) and south (Caine et al., 2017; Lisenbee, 2013) of the study area.

3. METHODS

3.1 Mapping and Structural Analysis

We characterized the IMSZ and related shear zones through 1:10,000-scale geologic mapping of an ~50 km^2 area and by collecting detailed structural data (Fig. 2; File S1[1]) documenting the orientation, thickness, length, kinematics, and structural context of outcrop and map-scale shear zones. Our study area includes the entire extent of the IMSZ, the southern end of the Crestone thrust, and the northern end of the Deadman Creek thrust (Fig. 2). The orientations of mapped shear zone margins and faults were calculated from three-point solutions along ~500–1000-m-long segments using a custom Python-based Quantum GIS (QGIS) tool utilizing elevation data from a 1-m resolution digital elevation model base map from U.S. Geological Survey 3DEP lidar data. For details on mapping, geospatial, and structural data collection methods, see Sitar (2023).

Petrographic analysis of ~30 samples evaluated microscale kinematics and deformation conditions (File S2). Microstructural kinematic indicators in oriented X:Z petrographic sections (perpendicular to foliation and parallel to lineation) include S-C fabrics, C′ shear bands, sheared veins, and oblique fabrics defined by recrystallized grain orientations in quartz ribbons. The modal percentage and dominant mineralogy of phyllosilicates were estimated for each sample, along with the relative extent to which phyllosilicates and quartz (rheologically weak phases) are interconnected at the thin section scale, which may govern the bulk rheology of polymineralogic rocks (e.g., Handy 1990). In some cases, estimates of phyllosilicate modal percentages were obtained directly from quantitative analyses by using a TESCAN integrated mineral analyzer (TIMA) at the Automated Mineralogy Lab at the Colorado School of Mines (File S3A). Phyllosilicate phases were identified in select samples using a TerraSpec Halo near-infrared spectrometer. Four quartz-rich samples were analyzed via electron backscatter diffraction (EBSD) at Washington and Lee University using a Zeiss EVO MA 15 scanning electron microscope operating in low vacuum at an accelerating voltage of 25 kV, probe current of 20–25 nA, and working distance between 15 mm and 25 mm. Step sizes between 0.5 µm and

[1]Supplemental Material. 1:10,000-scale geologic map (File S1); locations and descriptions of all samples (File S2); mineralogy and monazite scans (File S3); zircon U-Pb data (File S4); zircon fission track data (File S5); and monazite U-Th-Pb data (File S6). Please visit https://doi.org/10.1130/GEOS.S.28474307 to access the supplemental material, and contact editing@geosociety.org with any questions

20 µm were chosen on a sample-to-sample basis. Crystallographic axes were reduced to one point per grain and plotted on lower hemisphere pole figures.

3.2 Geochronology and Thermochronology

We used U-Pb geochronology and fission-track thermochronology to constrain the age of the shear zones. One mapped gabbro stock was analyzed via zircon U-Pb laser ablation–inductively coupled plasma–mass spectrometry (LA-ICP-MS) at the GeoAnalytical Lab at Washington State University, and zircon fission-track thermochronology under the direction of Paul O'Sullivan at GeoSep Services (Files S4 and S5). In both analyses, a laser spot size of 20 µm was used for U-Pb analyses. Seven polished thick sections of rocks from shear zones in the study area that include probable synkinematic to late synkinematic calcite veins were analyzed via LA-ICP-MS at the University of California, Santa Barbara, petrochronology facility to attempt to constrain their latest shearing with calcite U-Pb dates. Unfortunately, calcite in these samples did not contain sufficient U compared to common Pb to yield meaningful ages (Sitar, 2023). Grains of synkinematic to postkinematic monazite were identified in three polished thin sections from shear zones via TIMA analysis (File S3B), followed by reflected-light petrographic examination. These grains were dated via U-Th-Pb LA-ICP-MS analysis at the University of California, Santa Barbara. A spot size of 8 µm was used to maximize the number of spots and grains datable in each section (File S6). Analysis was completed using a Photon Machines excimer 193 nm laser equipped with a HelEX cell, a Nu Instruments Plasma P3D multicollector ICP-MS (for U, Th, and Pb isotopes), and an Agilent 7700× quadrupole ICP-MS (for rare earth elements, Y, and Si) following the methods outlined in Kylander-Clark et al. (2013) and described in the Supplemental Material (File S6). Data were reduced using Iolite (Paton et al., 2011), and IsoplotR (Vermeesch, 2018) was used to calculate various geochronometric ages from LA-ICP-MS data and to plot the data.

4. SHEAR ZONES: FIELD RELATIONS AND MACROSTRUCTURAL ANALYSIS

4.1 Independence Mine Shear Zone

The IMSZ is exposed over a length of ~5 km, truncated by the Sangre de Cristo fault at its southern end, and concealed by Quaternary sediment at the northern end (Fig. 2, File S1). Rocks within the mapped IMSZ consist of chlorite-rich mylonites and ultramylonites, with minor, localized areas of protomylonite to mylonite dominated by quartz, feldspar, and white mica (i.e., muscovite, phengite, and/or illite, per near-infrared spectrometer analyses). Three-point solutions along the mapped trace of the IMSZ margins suggest that it is curviplanar. Dips range from 25° to 62°W to W-SW, with shallower dips at the northern and southern ends of the mapped exposure (e.g., calculated orientations of 181°, 32°W; 169°, 56°W; and 154°, 26°SW along the northernmost, central, and southernmost segments, respectively; Fig. 3). The true thickness of the IMSZ (perpendicular to the margins) ranges from 15 m to ~100 m. Although the IMSZ is bound on either side by different Proterozoic gneissic units along parts of its mapped exposure (Fig. 2), the complexity in the distribution of these units precludes estimation of displacement. The IMSZ is partially or fully hosted within gneissic amphibolite throughout the study area. In most locations, the IMSZ cuts across gneissic foliation defined by compositional layering and mineral orientation, which commonly strikes E-W to NE-SW, and dips steeply (Fig. 4A; see Sitar, 2023, for a detailed description of Proterozoic structures).

Mylonitic foliation defined by aligned phyllosilicates ± quartz bands and a lineation generally defined by elongated quartz grains and streaks of mica characterize fabrics in the IMSZ. Foliation is notably more thinly spaced and platy than gneissic foliation adjacent to the shear zone (Figs. 5A and 5B). Mylonitic foliation consistently dips ~15°–40°W-SW to W-NW, and lineation plunges approximately down-dip to the W-SW (Fig. 4B). In most areas, dips of mylonitic foliation are consistently ≥10° shallower than that of the calculated local orientation of the IMSZ margins (Fig. 3). Macroscale S-C fabrics with locally well-developed C′ shear bands are visible in most exposures of the IMSZ. Generally, these fabrics are consistent with top-SW (normal-sense) shear, but they locally suggest top-NE (thrust/reverse-sense) shear, most notably at the Independence Mine itself (Fig. 5B).

4.2 Other Shear Zones

Twelve additional discrete brittle-plastic shear zones were identified during mapping that appear to either splay from the IMSZ or trend subparallel to it (Figs. 2 and 3; File S1). Many of these shear zones were first mapped as faults by Clement (1952). All non- IMSZs identified are thinner (~1–25 m thick) and less laterally extensive (with mapped lengths between ~0.5 km and ~3.3 km) than the IMSZ and are herein referred to as smaller shear zones. Three-point calculations for the smaller shear zones indicate dips ranging from 29° to 67°W to W-SW (Fig. 3). As in the case of the IMSZ, many of the smaller shear zones appear to offset internal contacts within the gneissic basement of the study area, but these offsets are not useful for estimating total displacement or relative age given the complexity of the gneisses and their Proterozoic age. One shear zone cuts a distinct tholeiitic gabbro stock near Cottonwood Creek (see Figs. 6 and S1) that is hydrothermally altered but contains relict clinopyroxene and hornblende and has quenched margins along its intrusive contact with Proterozoic gneiss (Fig. 6; see Sitar, 2023, for geochemical data on this gabbro). Where the gabbro is cut by the shear zone, it displays a top-SW S-C fabric dominated by secondary white mica and chlorite. Some amount of normal-sense offset across this shear zone is likely, but its magnitude is uncertain based on the irregular borders of the gabbro intrusion (Fig. 2 cross section D–D′, and Fig. 6B). This gabbro yielded late Oligocene zircon U-Pb and fission-track dates (see Section 6.1).

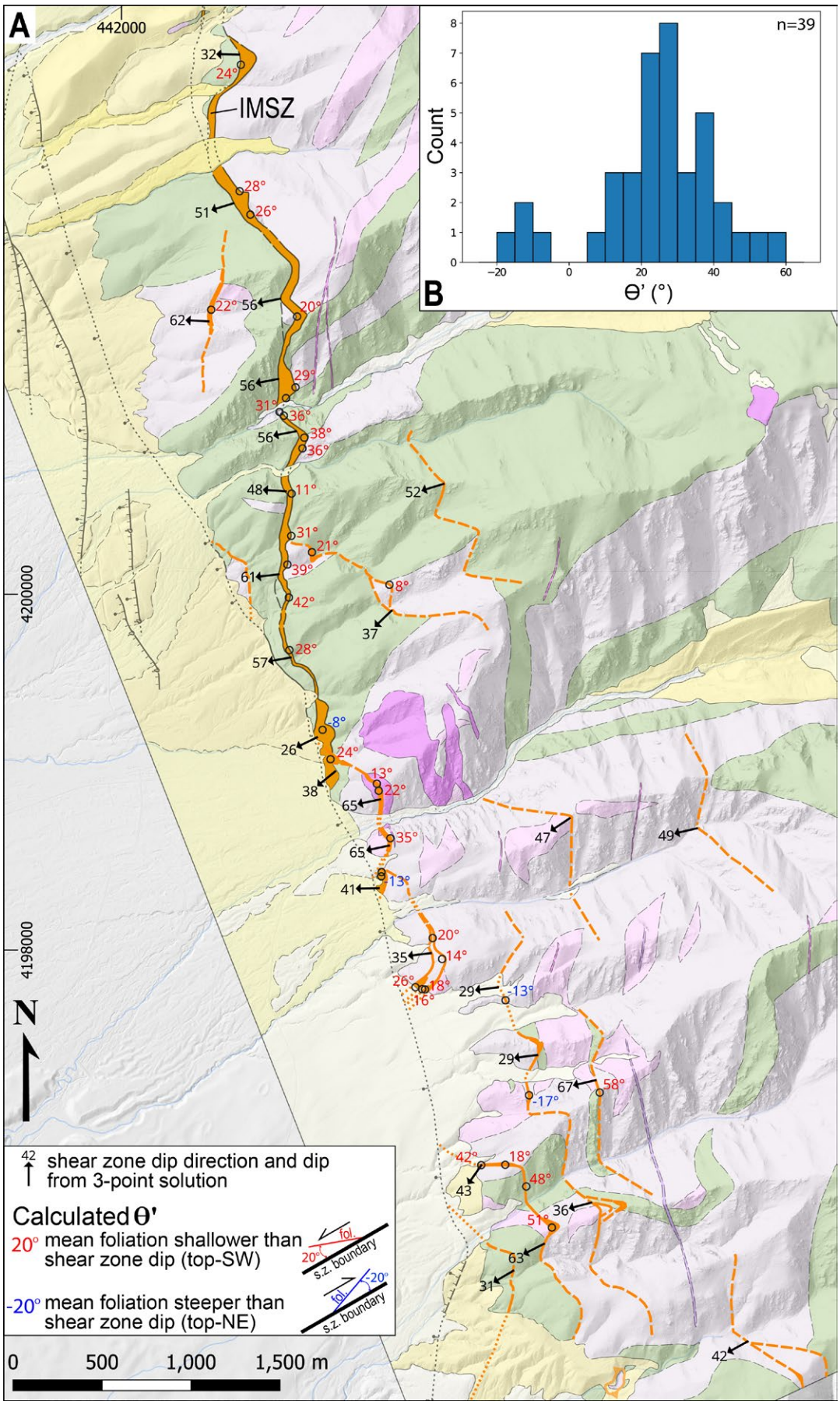

Figure 3. (A) Simplified geologic map of the Independence Mine shear zone (IMSZ) and related shear zones showing the calculated shear zone margin orientations from three-point solutions (black arrows indicate dip direction and dip) and angles between the shear zone margins and average foliation (θ′). Red θ′ values (positive) denote where foliation is shallower than the shear zone margin, consistent with top-SW shear, and blue θ′ values (negative) denote where foliation is steeper than the shear zone margin, consistent with top-NE shear. (B) Histogram of all calculated θ′ angles.

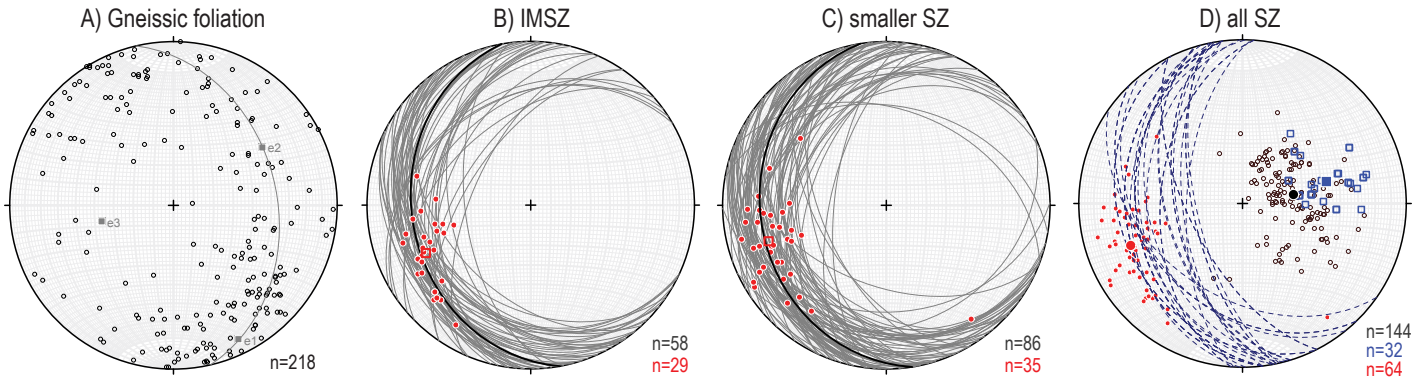

Figure 4. Lower hemisphere equal area plots of fabrics within the Proterozoic basement. (A) Poles to gneissic foliation with cylindrical best fit (gray great circle); e1 (maximum eigenvector): 154°, 10° (0.56; trend, plunge, eigenvalue), e3 (minimum eigenvector): 257°, 53° (0.15); e2 is the intermediate eigenvector. (B) Mylonitic foliation planes (gray) and lineations (red) in the Independence Mine shear zone (IMSZ). Bold black great circle is the mean plane (oriented 170°, 28°W). Red square is the mean lineation (oriented 245°, 30°). (C) Mylonitic foliation planes (gray) and lineations (red) in all other smaller shear zones. Bold black great circle is the mean plane (oriented 171°, 24°W). Red square is the mean lineation (oriented 253°, 26°). (D) Poles to all mylonitic shear zones (black circles) and lineations (red circles) and poles to shear zone margin orientations calculated from three-point solutions (dashed great circles and blue boxes as poles to planes). Large solid red circle is the mean lineation (oriented 249°, 28°). Large solid black circle is the mean foliation pole corresponding to a plane oriented 170°, 26°W. Solid blue box is the mean shear zone margin pole corresponding to a plane oriented 166°, 44°W. All plots were created using Stereonet software (Allmendinger et al., 2013).

The smaller shear zones are primarily bounded by Proterozoic quartzofeldspathic gneiss or granitoid (Figs. 2 and 3). Shear zone lithology varies according to the local host rock: IMSZ–like chlorite-rich ultramylonite to mylonite (Fig. 5C) is most common where shear zones are hosted by gneissic amphibolite, and quartz-feldspar–rich protomylonite to mylonite (with foliation commonly defined by aligned bands of quartz, fractured feldspar, and/or white mica) is most common where shear zones are hosted by quartzofeldspathic rock (Figs. 2 and 3). Some areas of quartz-feldspar–rich protomylonite are found within the relatively discrete (meter-scale) boundaries of clearly identified smaller shear zones, but others appear in shear zones that are either not map scale or cannot be traced beyond a single exposure (File S1). Measured mylonitic foliation both within and outside of map-scale shear zones generally dips moderately to shallowly (~15°–45°) W to W-SW, with down-dip lineations plunging W to SW (Fig. 4C). No significant differences in mylonitic foliation and lineation orientations are apparent between chlorite-rich and quartz-feldspar–rich mylonites. As in the case of the IMSZ, shear zone boundaries generally cut across Proterozoic gneissic foliation, and measured mylonitic foliation is consistently ≥10° more shallowly dipping than the shear zone margins (Figs. 3 and 4D). Macroscale S-C fabrics and C′ shear bands are variably developed within the smaller shear zones, and these fabrics are locally compatible with top-SW (normal-sense) kinematics (Fig. 5C), top-NE (thrust-sense) kinematics, or both, with contrasting kinematics along strike in the same shear zone or even the same outcrop. Top-NE S-C fabrics appear more commonly in quartz-feldspar–rich protomylonites, especially outside of map-scale shear zones. Besides local variations in modal mineralogy and structural thickness, few substantive differences between the IMSZ and other shear zones are clear.

The northernmost exposure of the Deadman Creek thrust appears near the southern edge of the study area in an erosional window that is mostly obscured by Quaternary sediment (Fig. 2). Like the Crestone thrust at the northern end of the study area, the Deadman Creek thrust consists of Proterozoic basement rocks over a footwall consisting of Ordovician Harding Formation quartzite and carbonate rocks likely belonging to the Mississippian Leadville Formation. Unlike the Crestone thrust, this exposure of the Deadman Creek thrust is marked by a discrete, ≤10-m-thick zone of protomylonite to mylonite composed of a variably sheared mixture of hanging-wall gneiss, and footwall Harding Formation quartzite (File S1). Mylonitic foliation dips ~25°W-SW here, and outcrop-scale S-C fabrics are consistent with top-NE (thrust-sense) shear, with other local kinematic indicators including C shear bands and quartz sigmoids suggesting top-SW (normal-sense) shear (Fig. 5D).

4.3 Relation Between Shear Zones and the Sangre de Cristo Fault System

The Sangre de Cristo fault system is locally expressed as a network of normal faults that trace NW-SE to N-S along and off the range front within the study area (Fig. 2). These faults are inferred to dip to the southwest at moderate to steep angles, consistent with an ~60° dip based on modeling of seismic data by Kluth and Schaftenaar (1994). Scarps and aeromagnetic data

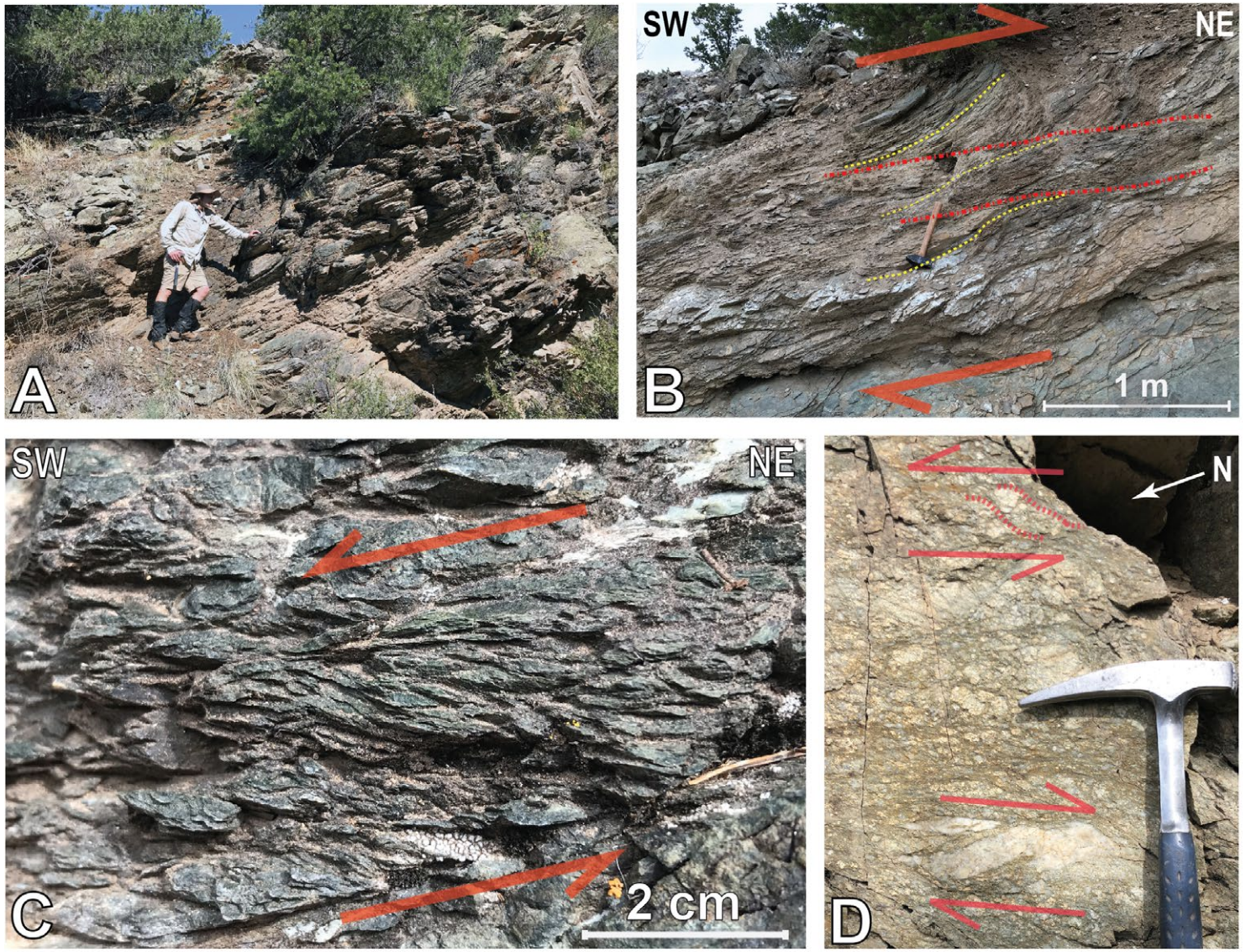

Figure 5. Photographs of shear zones in the study area. (A) Independence Mine shear zone (IMSZ) defined by chlorite-rich, gently SW-dipping foliation. (B) IMSZ at Independence Mine, with sigmoidal fabrics consistent with top-NE (reverse-sense) shear. (C) S-C fabrics, which are indicative of top-SW (normal-sense) shear in a chlorite-rich mylonite from a smaller shear zone. (D) Outcrop of the northernmost exposure of the Deadman Creek thrust/shear zone, with evidence of top-NE and top-SW shear based on sigmoidal foliation patterns.

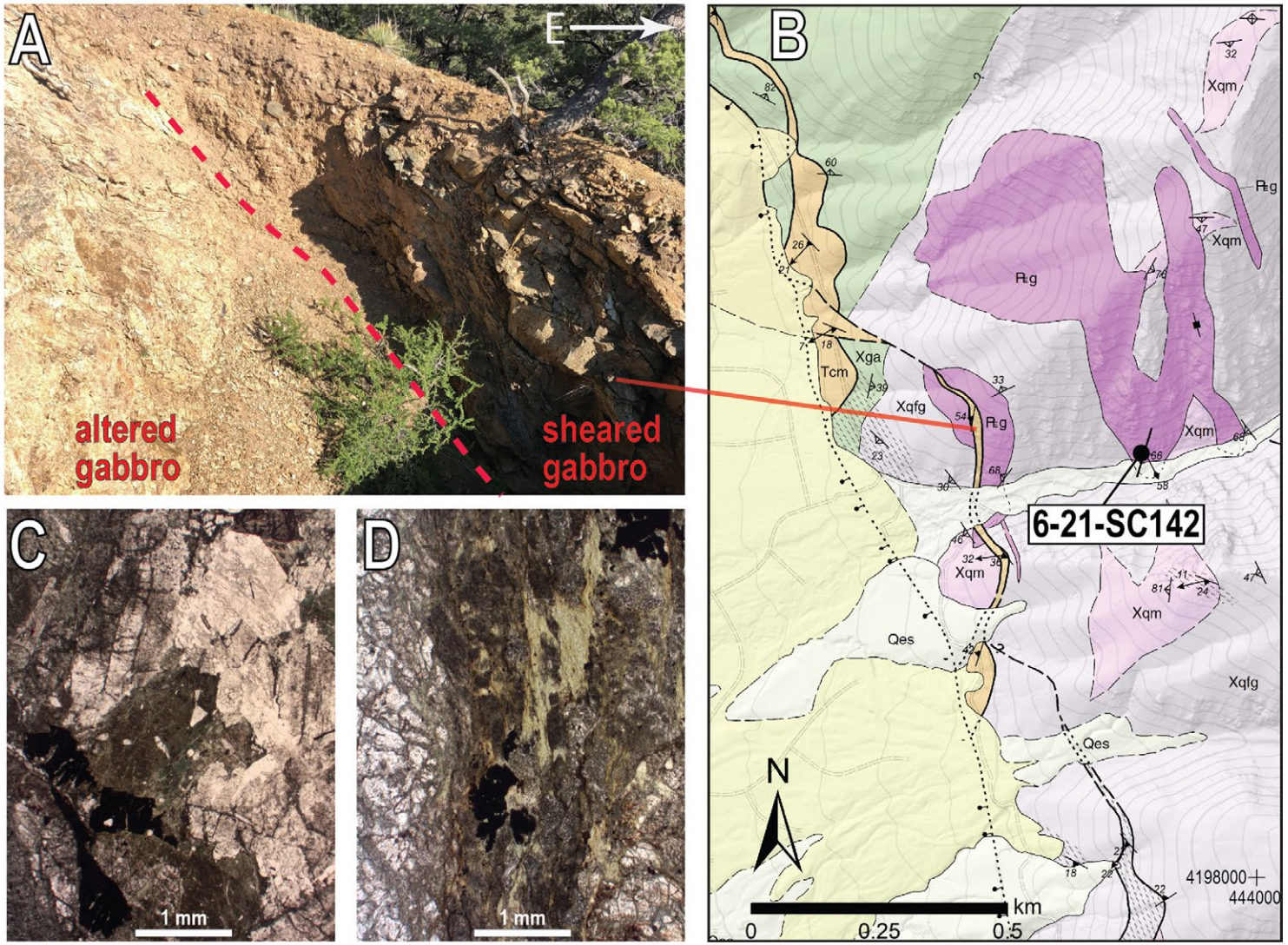

Figure 6. (A) Photograph of a prospect exposing altered late Oligocene gabbro with moderately SW-dipping mylonitic fabric. The dashed red line marks the boundary between sheared gabbro (to the right) and unstrained gabbro (to the left). (B) Geologic map of the gabbro unit (PEg) showing the location of the photograph in part A and sample 6-21-SC142, which was dated by zircon U-Pb and fission track analysis. See Figure 2 for map unit abbreviations. (C) Photomicrograph of the relatively unaltered gabbro at 6-21-SC142. (D) Photomicrograph of the gabbro where it is cut by the shear zone, showing intense fracturing and development of a foliation defined by chlorite.

suggest that faults off the range front commonly splay off or share relay ramps with a primary range-bounding fault (deemed the "Sangre de Cristo fault" for the purposes of this study) at the approximate edge of bedrock exposure in the study area (Fig. 2).

The Sangre de Cristo fault truncates all mapped mylonitic shear zones within the study area, including the IMSZ at its southern end (Figs. 2 and 3). The shear zones strike subparallel to and are more densely spaced toward the Sangre de Cristo fault and culminate in several discontinuous exposures of SW-dipping chlorite mylonite that appear within ~50 m of the range front. While this spatial relation could suggest a connection between the mylonites and the brittle Sangre de Cristo fault, we instead interpret these exposures as older shear zones that are cut by the more steeply dipping Sangre de Cristo fault system, based on their geometric differences and interpreted ages (see Section 7; Fig. 2; File S1).

5. MICROSTRUCTURAL ANALYSIS

5.1 Mineralogy and Textures

Petrographic samples from the IMSZ and other basement-hosted brittle-plastic shear zones vary in composition and degree of mylonitization, with samples ranging from protomylonitic quartz-feldspar–rich gneiss to chlorite ultramylonite. Protomylonitic rocks generally contain limited proportions (i.e., as little as ~1%) of white mica after feldspar, and quartz commonly represents the interconnected weak phase in these rocks. Most samples record various degrees of fracturing and brittle comminution of feldspar ± quartz, including samples that record exclusively top-SW shear and top-NE shear (e.g., Figs. 7A and 7B). Incipient sericitization of feldspar is commonly concentrated along brittle fractures (e.g., Fig. 7C), and proportions of white mica

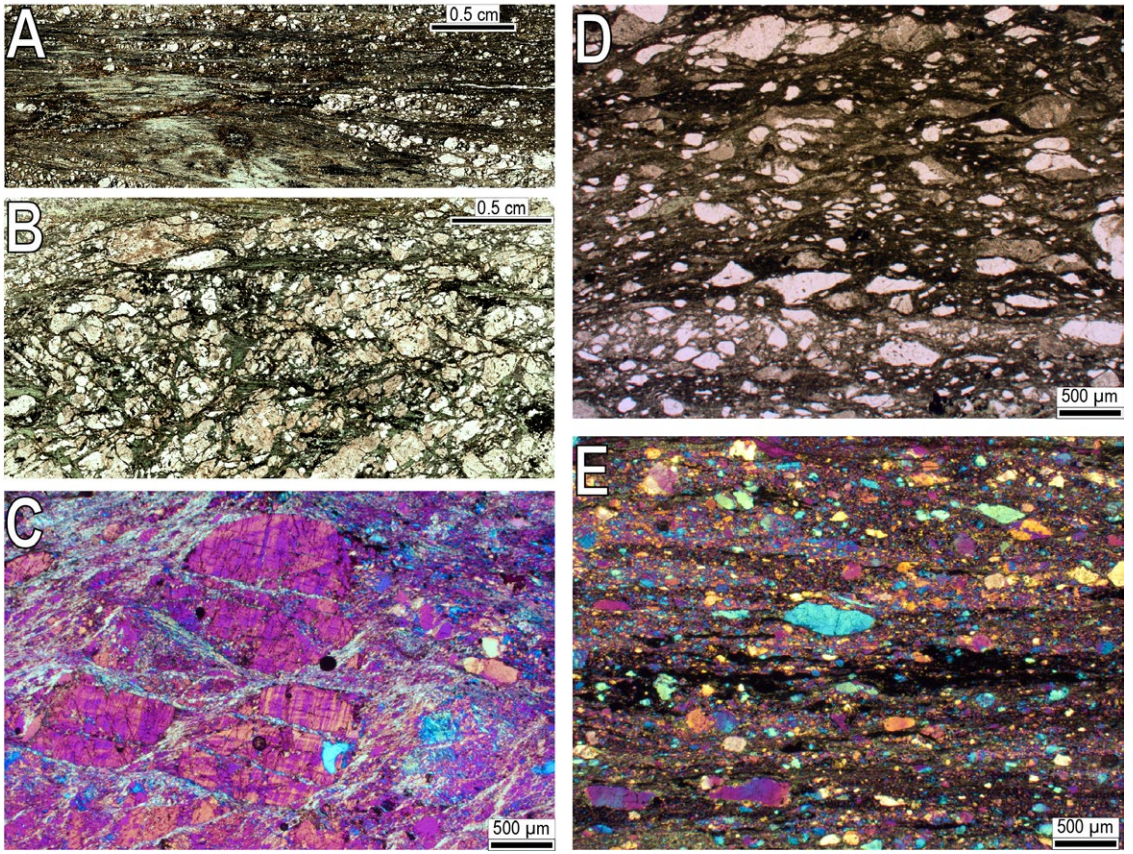

Figure 7. (A, B) Plane-polarized light scans and (C–E) photomicrographs of mylonites characterized by pervasive brittle deformation and development of secondary chlorite and white mica. All images are from X:Z sections with NE (up-plunge) on the right side. Images C and E were taken in cross-polarized light with the gypsum plate inserted. (A) Independence Mine shear zone (IMSZ) sample with top-SW S-C fabric (20-9-SC35). (B) Smaller shear zone protomylonite with top-NE S-C fabric (6-21-SC144). (C) Sample from the Deadman Creek shear zone with secondary white mica developed along fractured K-feldspar porphyroclasts (22-5-SC578). (D) IMSZ sample with elongate angular/subangular quartz porphyroclasts within a chlorite-rich matrix recording top-SW shear (19-7-14). (E) Smaller shear zone sample with quartz and feldspar porphyroclasts of highly variable sizes (6-21-SC149). File S2 provides locations of all thin sections; see text footnote 1.

and chlorite tend to increase with greater grain size reduction (Fig. 7). Chlorite, often in combination with white mica, is commonly a major component of more strained rocks (i.e., mylonite to ultramylonite). Although chlorite and white mica, in total amounts of ≤55%, usually form the interconnected weak phase of ultramylonitic samples, recrystallized quartz is interpreted to be the dominant interconnected weak phase in some high-strain mylonitic shear zone samples. Quartz and relict fractured and sericitized feldspar in variable proportions are the primary porphyroclasts. Quartz porphyroclasts, lenses, and smaller ribbons are commonly subangular and highly variable in size (Figs. 7D and 7E), and locally feldspar records pervasive cataclasis. These textures and deformation conditions suggest that many of the mylonitic shear zones evolved from cataclastic rock. Apatite, epidote, calcite, quartz, and iron oxide are common hydrothermal-metasomatic phases within mylonite-ultramylonite samples (File S2). Mutually crosscutting relations with shear fabrics indicate that the calcite, quartz, and iron oxide appear locally as synkinematic veinlets.

5.2 Kinematics

Microstructural kinematic indicators in shear zone samples are like those visible in outcrops, with top-NE mylonitic fabrics (Fig. 8) variably overprinted by top-SW S-C ± C′ fabrics (Fig. 9). Altogether, ~64% of oriented X:Z thin sections record exclusively to dominantly top-SW shear (locally with sparse and subtle indicators of top-NE shear); ~14% record exclusively top-NE shear, and ~21% record evidence of mixed top-SW and top-NE shear (Figs. 10A and 10B).

5.2.1 Reverse-Sense (Top-NE) Shear

Top-NE fabrics and domains preserving top-NE fabrics in samples with mixed kinematic indicators generally contain less phyllosilicate (~5%–20%) than those overprinted by top-SW fabrics (Fig. 10C). Rarely, mylonites with brittle-plastic fabrics and interconnected phyllosilicate exclusively record top-NE shear. Domains with kinematic indicators of top-NE shear disproportionately record quartz dynamic recrystallization compared to top-SW fabrics. In most samples with interpreted top-NE kinematics, ribbons of quartz are dominated by relatively small (~5–15 µm) recrystallized grains and subgrains with well-developed oblique grain-shape preferred orientations consistent with top-NE shear (e.g., Figs. 8C and 8D). Locally, quartz porphyroclasts and ribbon margins have randomly oriented <10-µm-wide bulges and recrystallized grains. These textures suggest a combination of subgrain rotation (SGR) and bulging (BLG) dynamic quartz recrystallization. BLG is probably more common within samples from the study area, but SGR accounts for a greater volume of quartz recrystallization where present. Quartz deformation in top-NE fabrics is not exclusively plastic; many samples record fracturing via angular quartz porphyroclasts with minor recrystallization, while others record late-kinematic brittle-plastic C′ shear bands that cut quartz ribbons (e.g., Fig. 8D). Other kinematic indicators besides S-C-C′ fabrics include mica fish, σ-porphyroclasts with mica tails, and sheared synkinematic to late kinematic calcite veinlets (Fig. 8F). Although top-NE–dominant samples tend to contain more quartz and feldspar than top-SW–dominant samples, some mylonite samples with consistent top-NE kinematic indicators display evidence of synkinematic chloritization (e.g., fractured porphyroclasts surrounded by chlorite or bound by high-strain, chlorite-rich C-foliations; Figs.7B and 8E). These samples suggest that, at least locally, the compositional frameworks of chlorite-rich, top-SW–dominant shear zones may predate their fabrics.

The northernmost exposure of the Deadman Creek thrust/shear zone records apparent top-SW kinematic indicators at the outcrop scale but clear top-NE indicators at the microscale. Top-NE kinematic indicators in this quartzofeldspathic mylonite/protomylonite include K-feldspar σ-type porphyroclasts with white mica tails, S-C-C′ fabrics in micaceous intervals (e.g., Fig. 8A), and antithetic (top-SW) shear bands at a high angle to foliation. Plastic deformation of quartz is limited to relatively minor BLG-SGR dynamic recrystallization in a minority of porphyroclasts. Lindsey and Caine (2024) also noted mixed top-NE and top-SW kinematic indicators in mylonite along the Deadman Creek shear zone just south of the study area at outcrop and microscopic scales.

5.2.2 Normal-Sense (Top-SW) Shear

The most characteristic microstructural kinematic indicators of top-SW fabrics in the study area are shear bands, usually either hosted within or lined by phyllosilicates (usually with more chlorite than white mica; Figs. 9A–9D). In several samples, C′ shear bands cutting top-NE S-C fabrics are the only indicators of top-SW overprinting. More common, however, are fully developed, phyllosilicate-dominated S-C-C′ fabrics without any relict indicators of top-NE kinematics. These fabrics may be dominant at an outcrop scale (as in much of the IMSZ) or limited to localized domains, high-strain zones, and/or shear bands where phyllosilicates form an interconnected weak phase. Greater modal proportions of phyllosilicates (20%–55%, usually mostly chlorite) appear to be correlated with top-SW shear (Fig. 10C). This pattern is also evident at an outcrop scale. For example, samples from the IMSZ at Independence Mine preserve top-NE shear in quartz-rich domains (Fig. 8B) but pervasive top-SW shear in chlorite-rich domains (Fig. 9B). Fabrics in several samples preserve quartz dynamic recrystallization with oblique grain shape-preferred orientations consistent with top-SW shear (e.g., Figs. 9E and 9F) and sigmoidal elongation of quartz porphyroclasts. Top-SW S-C-C′ fabrics are, however, also frequently associated with brittle fracturing of quartz fabrics (e.g., Fig. 9A). Systematic fracturing and rotation of relict feldspar porphyroclasts are also common top-SW kinematic indicators. Sheared late synkinematic calcite and Fe-oxide veins, mica fish, and σ-type porphyroclasts with chlorite-white mica tails are somewhat less common.

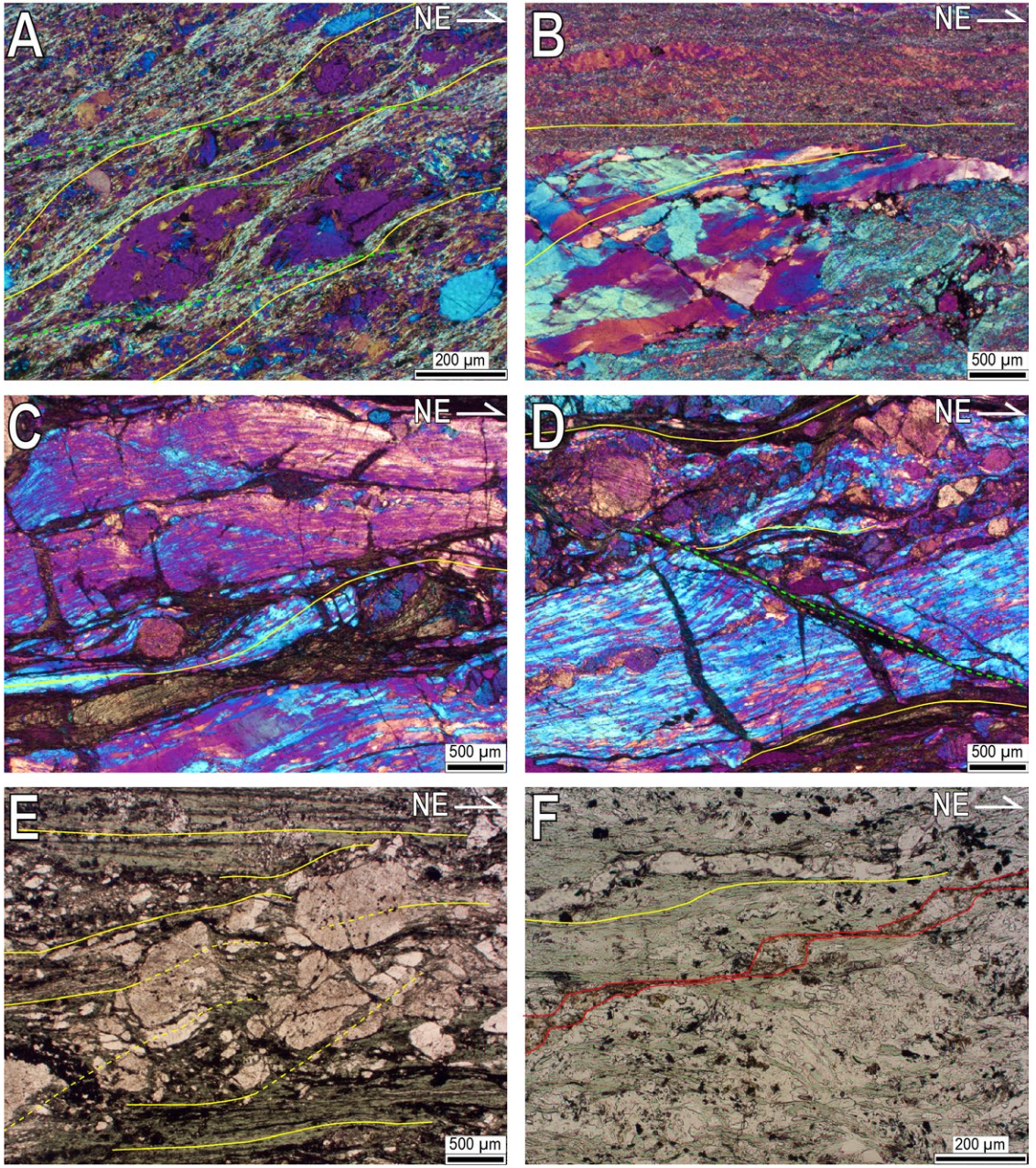

Figure 8. Photomicrographs of mylonite samples from the study area that record a top-NE sense of shear. All photomicrographs are from X:Z planes with NE (up-plunge) on the right. (A–D) Taken in cross-polarized light with gypsum plate inserted; (E, F) taken in plane-polarized light. Yellow lines are parallel to the trace of foliation. (A) S-C fabrics in a white mica-rich sample from Deadman Creek shear zone (22-5-SC578); dashed green lines trace C-planes. (B) Sigmoidal foliation patterns in quartz ribbons from a sample from the IMSZ (5-21-SC34). (C, D) S-C-C′ fabrics in quartz-rich sample from a non-IMSZ shear zone (5-21-SC29). Dashed green line in image D traces a brittle-plastic C′ shear band. (E) S-C fabrics in a chlorite-rich protomylonite from a smaller shear zone (6-21-SC144). (F) Sheared calcite vein (outlined in red) in a chlorite-rich sample from a smaller shear zone (21-5-SC58).

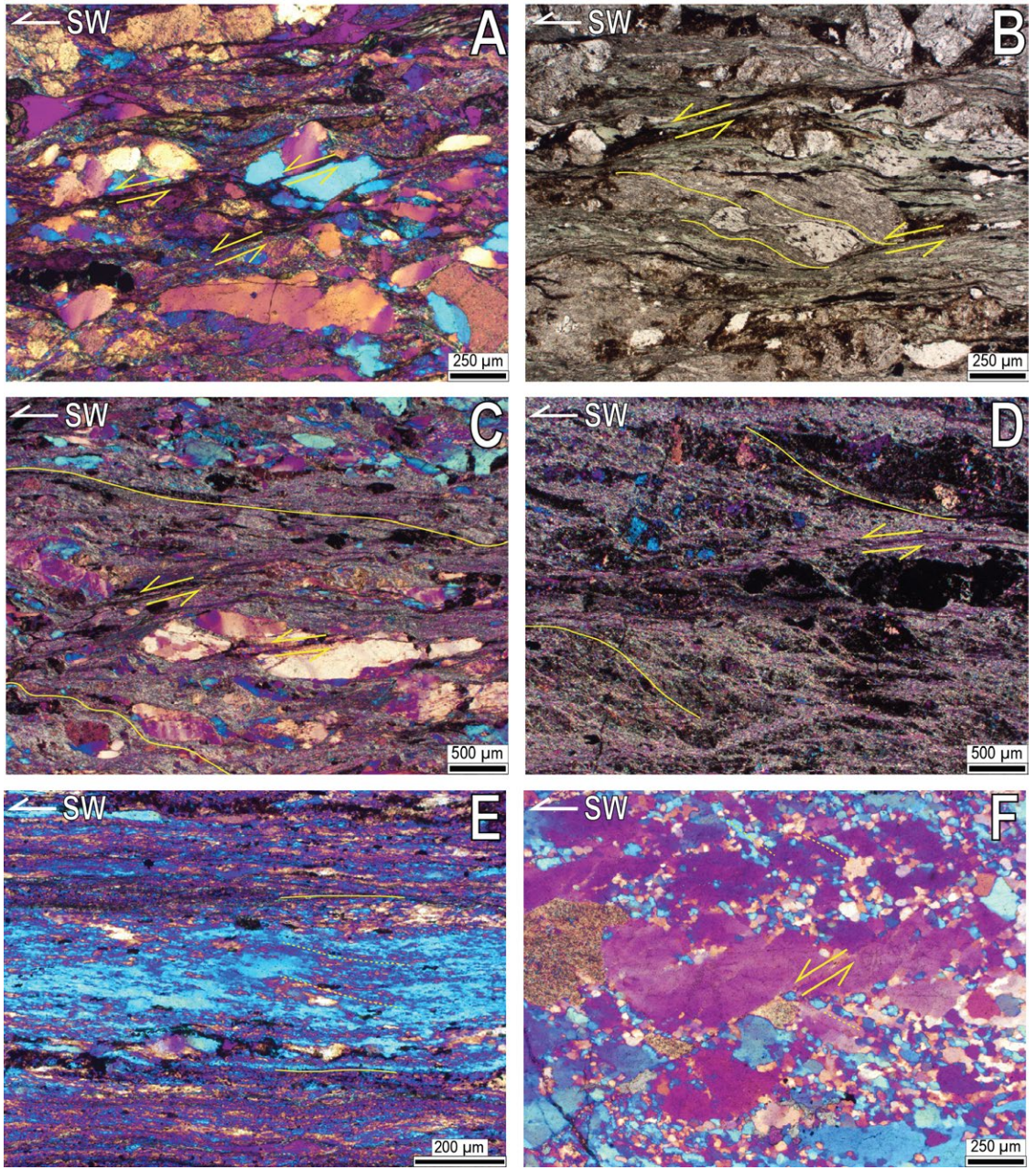

Figure 9. Photomicrographs of mylonite samples from the study area that record a top-SW sense of shear. All photomicrographs are from X:Z planes with SW (down-plunge) on the left and shown in cross-polarized light with a gypsum plate inserted, except for B, which is a plane-polarized image. Yellow lines trace foliation, and yellow arrows locally mark top-SW shear bands. (A) Brittle-plastic top-SW shear bands from the Independence Mine shear zone (IMSZ; 19-7-14). (B) S-C fabric in a chlorite-rich mylonite from the IMSZ (5-21-SC34). (C) S-C fabrics in a sample from a smaller shear zone (6-21-SC155). (D) S-C fabrics in a white mica-rich mylonite from a smaller shear zone (6-21-SC167). (E) Sample from the IMSZ (5-21-SC34) with a quartz lens recording variable dynamic recrystallization (center of image); dashed yellow lines trace a quartz grain shape fabric that is oblique to the overall foliation. (F) Dynamically recrystallized quartz from a boudinaged vein in a smaller shear zone (from the same outcrop as photograph in Fig. 5C; 5-21-SC12; yellow arrows mark a brittle-plastic top-SW shear band, and dashed yellow lines trace a grain shape fabric that is locally oblique to the overall subhorizontal foliation.

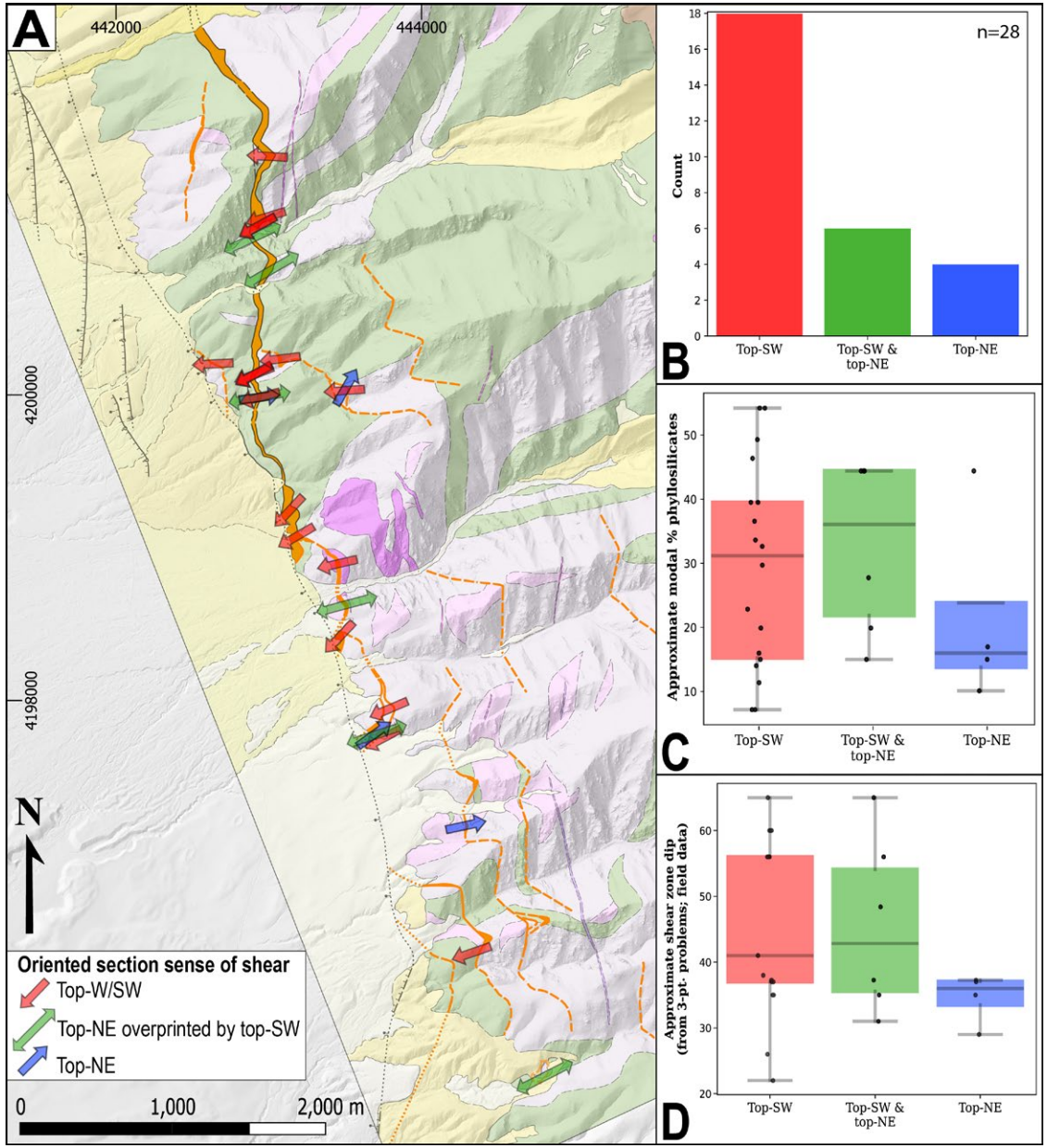

Figure 10. (A) Simplified geologic map of the Independence Mine shear zone and related shear zones showing the interpreted sense of shear with arrows parallel to lineation directions (blue—top-NE reverse-sense shear; red—top-W/SW normal-sense shear, green—top-NE shear overprinted by top-SW shear). (B) Histogram showing number of oriented thin sections that record top-SW shear (red), mixed kinematics (green), or top-NE shear (blue). (C) Box and whisker plot of the modal % phyllosilicates (chlorite and white mica) correlated with shear sense. (D) Box and whisker plot of the shear zone margin dip correlated with shear sense.

5.3 Electron Backscatter Diffraction Analysis of Quartz Crystallographic Fabrics

EBSD analyses of quartz in four mylonite samples from the IMSZ and related shear zones all yielded crystallographic preferred orientations (CPOs) with variable strengths and asymmetries (Fig. 11A). Despite differences in crystallographic fabric patterns, misorientation data for all samples are indicative of quartz basal <a> slip (Fig. 11B), which is typically the dominant slip system in relatively low-temperature dislocation creep regimes (e.g., Passchier and Trouw, 2005). Sample 5-21-SC34c is a quartz- and white mica–rich mylonite from the IMSZ at the Independence Mine. Microstructural kinematic indicators in this sample are mixed, with sigmoidal quartz ribbons and shear bands recording dominant top-NE shear (Fig. 8B) and much more localized domains of foliation and grain-shape preferred orientation patterns compatible with top-SW shear. EBSD analysis targeted two quartz-rich areas within the dominant top-NE domains. The pole figure for sample 05-21-SC34c is asymmetric, with a c-axis girdle and a-axes distribution compatible with top-NE, simple-dominated shear (Fig. 11). Sample 19-7-14 is a chlorite mylonite from the IMSZ. It has a well-developed, chlorite-dominated top-SW S-C-C′ fabric and isolated elliptical quartz grains that locally display minor domains of dynamic recrystallization and have been fractured along top-SW C′ bands (Fig. 9A). EBSD analysis targeted a wide area across the thin section, with most data coming from the elliptical quartz clasts aligned parallel to foliation. Despite the clear top-SW S-C-C′ fabric in sample 19-7-14, the distribution of quartz c-axes is slightly asymmetric with respect to foliation, and compatible with a component of top-NE shear (Fig. 11).

Sample 5-21-SC29 is a quartz-feldspar-chlorite protomylonite from a thin SW-dipping shear zone structurally below the IMSZ. Outcrop scale-kinematic indicators locally record top-SW shear, but the sample is dominated by top-NE S-C fabrics and brittle-plastic shear bands (Figs. 8C and 8D). Quartz ribbons record moderate degrees of SGR + BLG recrystallization, whereas feldspar is pervasively fractured. The sample has a strong quartz CPO characterized by a single c-axis girdle and a-axes maxima oriented clockwise to the foliation, which is compatible with top-NE shear (Fig. 11). Sample 20-9-SC34 is a quartz-dominated ultramylonite collected at the mapped intersection between a smaller shear zone and the Sangre de Cristo fault strand at the topographic base of the range. Quartz is pervasively recrystallized via SGR + BLG, and oblique foliation and grain shape orientation patterns and C′ shear bands record top-SW shear. Fabrics are cut by variably recrystallized quartz veins with an orientation consistent with a top-SW strain regime. EBSD analyses of multiple quartz ribbons yielded a moderately defined quartz CPO with a broad c-axis girdle and two maxima forming an ~57° opening angle near the Z-axis (Fig. 11). The girdle is slightly asymmetric, with a distribution of c- and a-axes that is consistent with top-SW shear. The c-axis opening angle suggests a deformation temperature of ~440 ± 50 °C, using the calibration of Faleiros et al. (2016).

6. GEOCHRONOLOGY AND THERMOCHRONOLOGY

6.1 Zircon U-Pb and Fission Track Data

LA-ICP-MS U-Pb analysis of zircon grains separated from a sample of the gabbro stock cut by a brittle-plastic shear zone (sample 06-21-SC142, located in the footwall of the shear zone; Fig. 6) yielded 26 concordant dates ranging from the Paleoproterozoic to late Oligocene, with inherited subpopulations from the Paleoproterozoic (ca. 2500–1658 Ma; n = 4), Mesoproterozoic (ca. 1525–1054 Ma; n = 4), and Neoproterozoic to Ordovician (ca. 581–472 Ma; n = 9). The youngest population (n = 9) consists of <60-µm-wide grains that yielded a weighted mean age of 25.7 ± 1.0 Ma (±2σ), with a relatively high mean square of weighted deviates (MSWD) of 6.1 (Figs. 12A and 12B). The two youngest grains do not overlap several of the other grains in this population at 2σ and thus may record minor Pb loss (Figs. 12A and 12B). If these grains are excluded, the weighted mean age is 26.7 ± 0.5 Ma, with a low MSWD of 0.9. Regardless of how the age is interpreted, these zircon U-Pb data provide a late Oligocene upper age constraint on the latest normal-sense shear along the brittle-plastic shear zone cutting this stock. Fission-track analyses of 19 zircon grains from the same sample yielded a pooled fission-track age of 26.7 + 3.6/–3.2 Ma (Fig. 12C). Only two of these grains have corresponding Oligocene U-Pb dates; most other grains have Cambrian to Mesoproterozoic U-Pb dates. These fission-track data indicate that the stock had cooled below ~200–260 °C (approximate zircon fission-track closure temperature range, e.g., Reiners and Brandon, 2006) before the beginning of the Miocene (ca. 23.5 Ma at latest; <~2.8 m.y. after emplacement).

6.2 Monazite U-Th-Pb

U-Pb LA-ICP-MS analyses of monazite from three mylonite samples (Files S3B and S5) yielded high common Pb values that are characteristic of hydrothermal monazite (e.g., Janots et al., 2012), and we interpret crystallization ages as lower intercept discordia ages on Terra-Wasserburg diagrams (Fig. 13). A sample from the IMSZ at Spanish Creek (20-9-SC31; Fig. 2) contains a population of small (≤50 µm) monazite grains, which are mostly located along mylonitic foliation or top-SW C shear bands and found in close association with Fe-oxide veinlets. The veinlets appear to have a mutually crosscutting relation with the top-SW C shear bands, where they (along with associated monazite) are commonly either sheared or completely dissected. We interpret the monazite as metasomatic and late synkinematic to top-SW displacement on the IMSZ. LA-ICP-MS U-Th-Pb dating of monazite from this sample yielded dates from 16 spots, most of which have low Th contents (<200 ppm for most spots; Fig. 13). Three spots were discarded from the discordia age calculation due to anomalously low $^{207}Pb/^{206}Pb$. Two of these spots were on the same grain and may have been placed too close to the margins of the target monazites. The remaining analyses produced a calculated lower intercept age of 24.4 ± 3.1 Ma

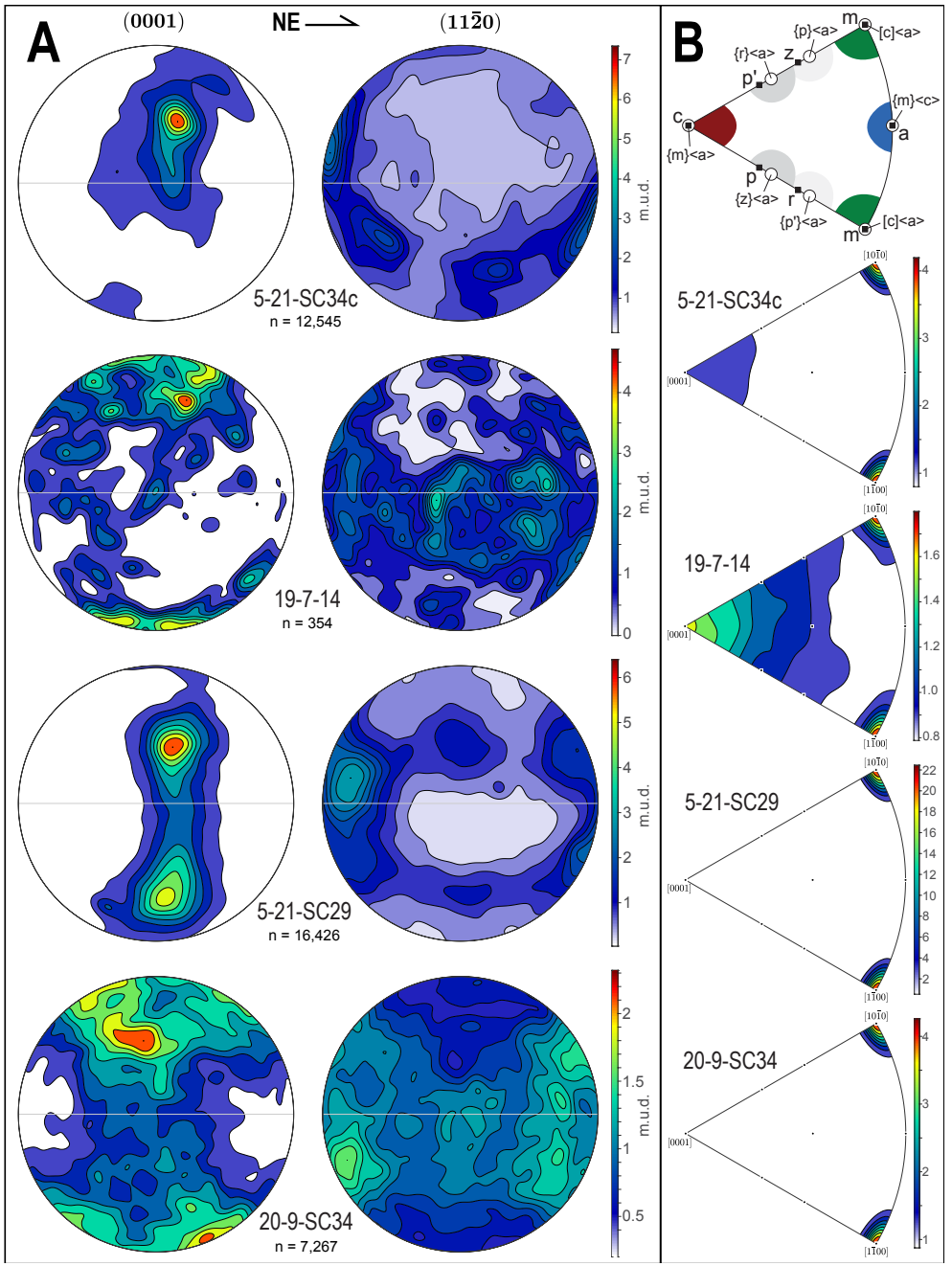

Figure 11. Quartz electron backscatter diffraction data from mylonite samples. (A) Lower hemisphere pole figures of quartz c-axes (0001) and a-axes (11–20) from samples 5-21-SC34, 19-7-14, 5-21-SC29, and 20-9-SC34. Data are presented in the X:Z reference frame with the NE end of the X-axis (lineation) on the right; m.u.d.—multiples of uniform distribution contour interval; n—number of grains analyzed. (B) Inverse pole figures showing the contoured distribution of misorientation axes with respect to crystallographic axes in m.u.d. Top figure is a reference modified from Neumann (2000) correlating misorientation axes with crystallographic slip systems. These data indicate a dominance of basal <a> slip ([c] <c>), with a minor component of prism <a> slip ({m}<a>) in 5-21-SC34c and 19-7-14.

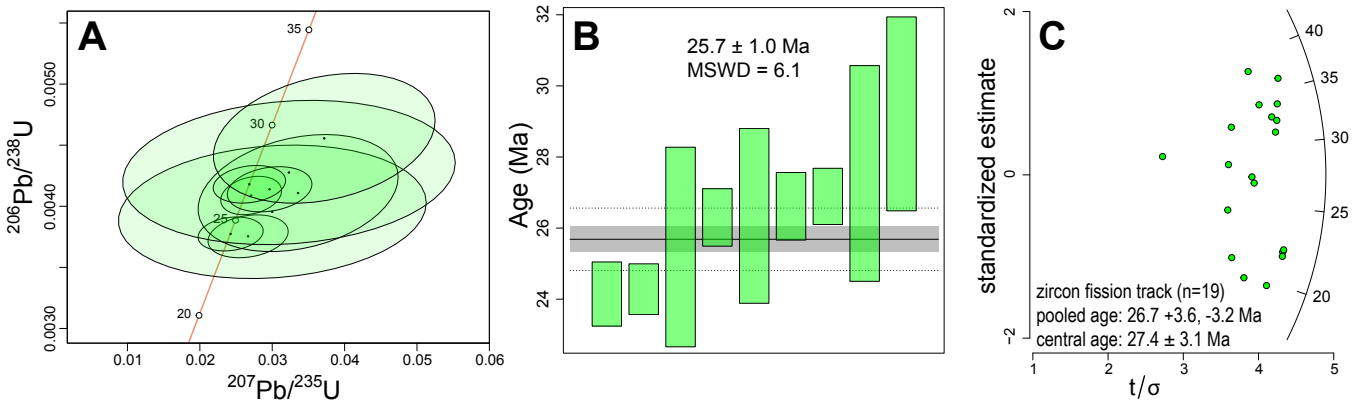

Figure 12. Zircon U-Pb and fission-track data from gabbro sample 6-21-SC142 (see Fig. 6B for location; sample coordinates: 37.93530°N, 105.63976°W). (A) Wetherill U-Pb concordia diagram focused on the youngest nine zircons. (B) Weighted mean U^{238}/Pb^{206} age plot. (C) Zircon fission track radial plot. MSWD—mean square of weighted deviates.

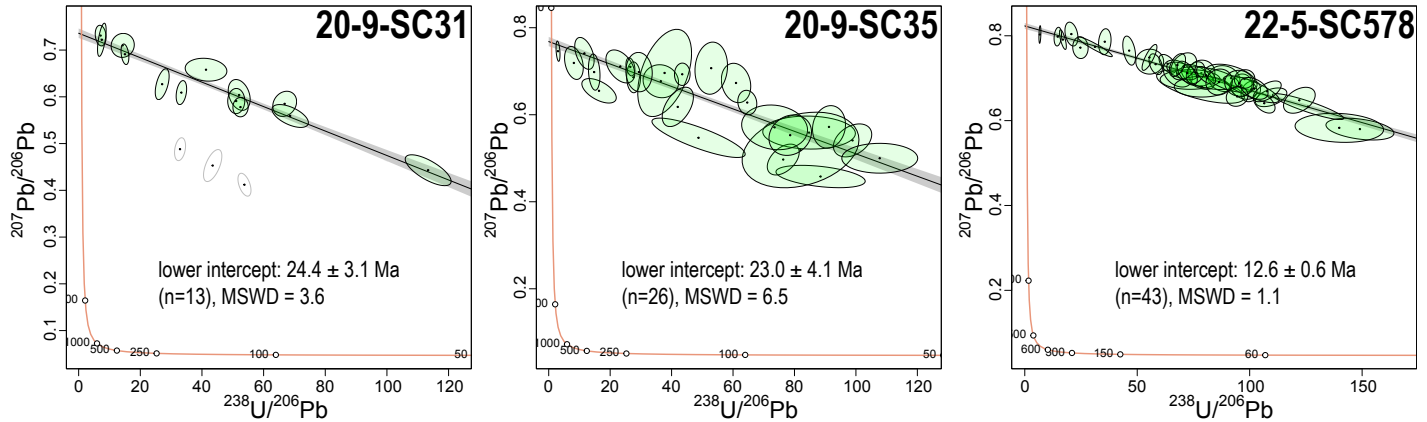

Figure 13. Tera-Wasserburg concordia diagram of monazite U-Pb data from samples 20-9-SC31 (coordinates: 37.95504°N, 105.65005°W), 20-9-SC35 (coordinates: 37.93894°N, 105.64720°W), and 22-5-SC578 (coordinates: 37.90573°N, 105.62786°W). See Figure 2 for sample locations. MSWD—mean square of weighted deviates.

(MSWD = 3.6; Fig. 13). A likewise high initial Pb value ($^{207}Pb/^{206}Pb_o$) of ~0.754 suggests a possibility of inheritance from older monazite and that the actual age of these grains could be younger. Local normal-sense displacement along the IMSZ is thus constrained to the latest Oligocene to earliest Miocene.

Sample 20-9-SC35 is of a chlorite-rich mylonite outcrop at the intersection between the IMSZ and the Sangre de Cristo fault system (Figs. 2 and 7A). Similar to sample 20-9-SC31, monazite in 20-9-SC35 commonly occurs in association with rutile-rich layers entrained along foliation and top-SW shear bands, and within sheared Fe-oxide veinlets, which suggests that the monazite is also late synkinematic. LA-ICP-MS U-Th-Pb dating of these monazite grains yielded dates from 26 spots (Fig. 13). These data are relatively scattered in the Tera-Wasserburg plot, with extremely old calculated ^{232}Th-^{208}Pb ages for spots with low (<200) $^{208}Pb/^{204}Pb$, which yielded a relatively imprecise lower intercept discordia age of 23.0 ± 4.1 Ma (MSWD = 6.5; Fig. 13). A weighted mean of ^{232}Th-^{208}Pb dates (n = 13, after discarding 13 analyses with $^{208}Pb/^{204}Pb$ < 200 or $^{232}Th/^{238}U$ < 100) was used to obtain a statistically more robust sample age of

22.1 ± 0.7 Ma. In any case, the 20-9-SC35 monazite U-Th-Pb data constrain latest normal-sense plastic shear on this part of the IMSZ to the earliest Miocene.

Sample 22-5-SC578 is a mylonitic Proterozoic granitoid from along the northernmost exposure of the Deadman Creek thrust, which is located ~1 km east of the Sangre de Cristo fault and ~3 km southeast of the southernmost exposure of the IMSZ (Fig. 2). This sample records abundant (~45%) secondary white mica and top-NE–directed (thrust-sense) S-C-C′ fabrics (Fig. 8A). Monazite grains in this sample have irregular shapes, are commonly oriented at a high angle to foliation, and have inclusions of other phases aligned with the foliation, which suggests that the monazite is postkinematic with respect to the main fabric. LA-ICP-MS analyses of 43 monazite grains from this sample indicate relatively low U (average of ~290 ppm U) and high common Pb. U-Pb analyses define a well-constrained Tera-Wasserburg lower intercept age of 12.6 ± 0.6 Ma (MSWD = 1.1; Fig. 13). We interpret this age to record postkinematic fluid flow that is most likely associated with the Sangre de Cristo fault system, which is associated with an abrupt increase in rapid cooling across the range in the Middle Miocene (Singleton et al., 2024).

7. DISCUSSION

7.1 Structural Evolution of Brittle-Plastic Shear Zones in the Sangre de Cristo Range

7.1.1 Reverse-Sense Shear

Detailed mapping of the IMSZ expands on the work of Clement (1952) and Lindsey et al. (1986b) and identifies the IMSZ as being the locally thickest and most laterally extensive member of a system of brittle-plastic shear zones. These shear zones are along strike with or structurally above the Deadman Creek thrust/shear zone, which shows evidence of top-NE shear consistent with regional Laramide shortening and top-SW shear consistent with Rio Grande rift extension (Lindsey and Caine, 2024). Many of the thrust/reverse faults in the Sangre de Cristo Range could have initiated during shortening of the Ancestral Rocky Mountains, but direct evidence (e.g., thrust deformation of Mesozoic units along the eastern flank) and more indirect evidence (e.g., thrust deformation of the entire exposed Pennsylvanian–Permian section) support the interpretation that major structures such as the Deadman Creek thrust/shear zone record Laramide shortening (Lindsey and Caine, 2024). The northernmost exposure of protomylonite-cataclasite along the Deadman Creek shear zone identified in this study also records macro- and micro-structural indicators of top-NE shear in addition to localized evidence of top-SW shear (Figs. 5D and 8A). Evidence from mapping and microstructural work of the IMSZ and smaller, related shear zones broadly supports top-NE kinematics consistent with Laramide origins for these brittle-plastic shear zones without precluding or substantiating origins during the Ancestral Rocky Mountains orogeny (Fig. 8). Top-NE displacement magnitudes along brittle-plastic shear zones are effectively unconstrained, but decameter-scale zones of mylonite to ultramylonite imply that these displacements may have been significant.

Inconsistent overprinting relations between plastic quartz deformation (e.g., dynamic recrystallization and formation of ribbons) and brittle fracturing is apparent in top-NE shear fabrics from the study area, which suggests spatio-temporal variability between shear zones and the brittle-plastic transition during top-NE shear. All brittle-plastic shear zones in the study area are in Proterozoic rocks in the hanging wall(s) of either the Crestone thrust or the younger (presumably Laramide) Sand Creek thrust fault. Greenschist-facies metamorphic assemblages (chlorite, white mica, and epidote ± calcite) and evidence of quartz dislocation creep and basal <a> slip preserved in top-NE fabrics suggest deformation temperatures ≥~300 °C. However, deformation temperatures likely did not greatly exceed this value, given the mixed plastic and brittle deformation of quartz (e.g., Figs. 7D and 8D). Taken together, these observations indicate deformation near the lower limit of quartz plasticity during top-NE shear. Assuming the 30 °C/km Laramide geothermal gradient used by Lindsey et al. (1986b), a depth of ~10 km is likely for basement rocks exposed along the western flank of the range during top-NE reverse-sense shear.

Given evidence of a brittle precursor to plastic quartz deformation associated with top-NE shear, the IMSZ and related smaller shear zones may have initiated as cataclastic fault zones to accommodate early Laramide shortening at depths above the brittle-plastic transition. They may then have been buried under since-eroded thrust sheets to depths at or below the brittle-plastic transition. Greenschist-facies assemblages and shear-involved veinlets (typically calcite, quartz, and Fe-oxide) suggest concurrent burial-associated heating and contact with fluid, and hydrolytic weakening may have helped to facilitate dislocation creep at relatively low temperatures (Fig. 14A). Mylonitic fabrics characterized by plastic deformation of quartz could then have formed concurrently with continued top-NE shear, with advanced lower greenschist-facies alteration facilitated within shear zones by local fracturing and fluid channelization. Finally, plastic quartz fabrics could have been locally overprinted by top-NE brittle deformation due to subsequent unroofing, increases in strain rate, or some combination thereof.

7.1.2 Normal-Sense Shear

Macro- and micro-structural evidence indicates widespread top-SW extensional reactivation of the IMSZ and related brittle-plastic shear zones along the western flank of the Sangre de Cristo Range. Outcrop-scale kinematic indicators at the northern end of the Deadman Creek thrust and recent work by Lindsey and Caine (2024) indicate that this shear zone also records extensional reactivation. By contrast, no clear macro- or micro-structural indicators of extensional reactivation of the Crestone thrust system were identified in the map area. An undeformed Oligocene (?) rhyolitic dike intruded along the Crestone thrust near the north end of the study area (Fig. 2, File S1) and a

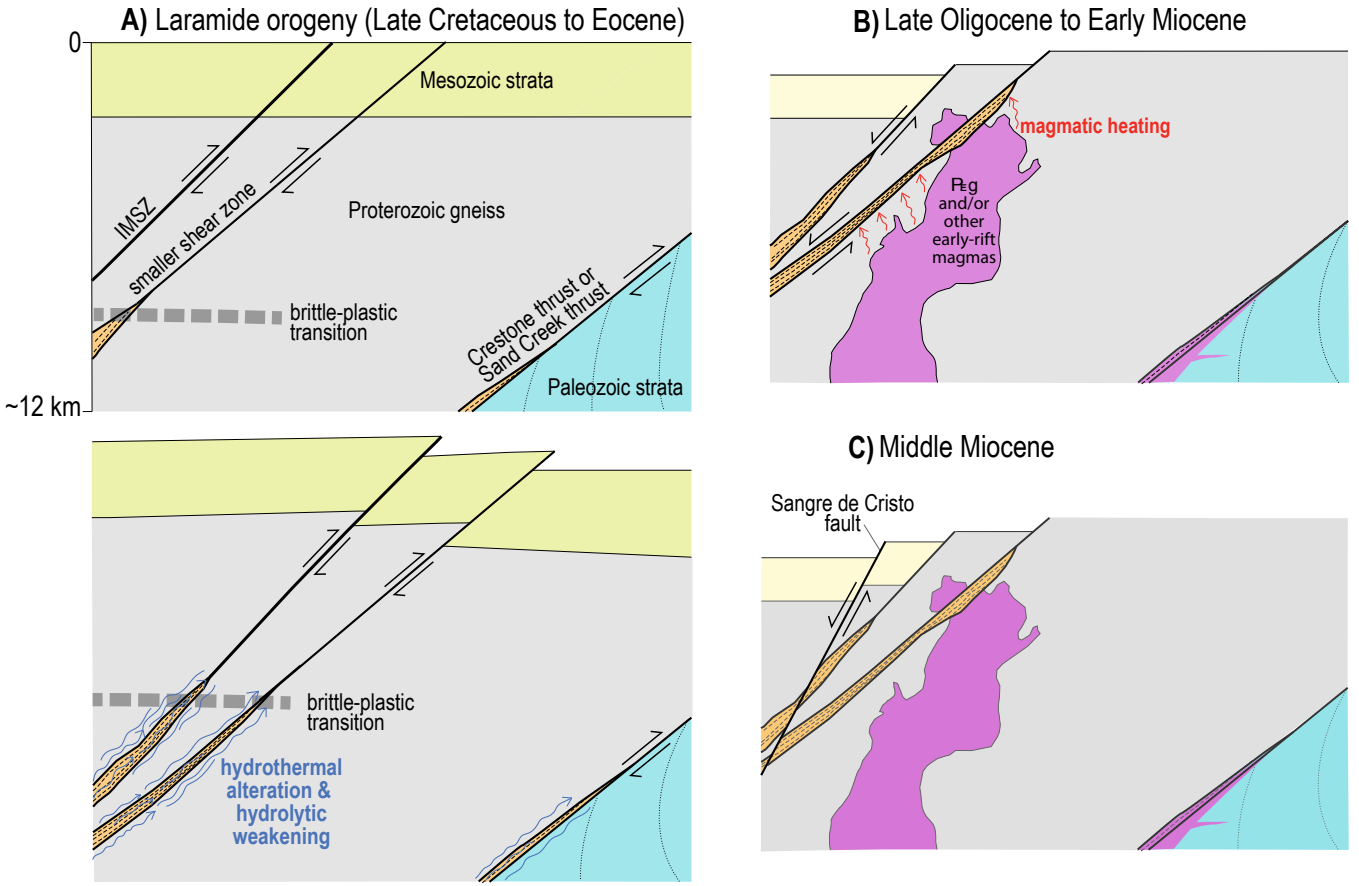

Figure 14. Schematic cross sections showing the interpreted structural evolution of the Independence Mine shear zone (IMSZ) and related shear zones during the Late Cretaceous to Middle Miocene.

similar relation mapped by Lindsey et al. (1985) farther to the north also provide strong evidence of a lack of post-Laramide displacement. These rhyolitic dikes resemble a ca. 27 Ma dike dated by Holm-Denoma et al. (2019) in the Deadman Creek area. Small-displacement fault planes with quartz slickenfibers in the Minturn Formation in the footwall of the Crestone thrust record slip consistent with an overall top-NE thrust-sense regime (Sitar, 2023).

Zircon U-Pb dating of the sheared gabbro intrusion provides a robust latest Oligocene to earliest Miocene (25.7 ± 1.0 Ma) maximum age constraint for the latest top-SW shearing in one brittle-plastic shear zone in the study area (Figs. 6 and 12). This age is approximately synchronous with the timing of early Rio Grande rift extension in the vicinity of the Sangre de Cristo Range, as interpreted by previous studies (e.g., Wallace, 2004; Ricketts et al., 2016). Age constraints from U-Th-Pb dating of synkinematic to late kinematic monazite (24.4 ± 3.1 Ma from 20 to 9-SC31 and 23.0 ± 4.1 Ma from 20 to 9-SC35) provide additional evidence of late Oligocene to Early Miocene normal-sense displacement (Fig. 14B). These analyses have high MSWD values (Fig. 13), but the weighted mean ^{232}Th-^{208}Pb date from 20 to 9-SC35 (22.1 ± 0.7 Ma) appears to be robust. Regardless, extensional displacement along the reactivated brittle-plastic shear zones was ongoing during synkinematic monazite development in the late Oligocene to earliest Miocene, prior to the apparent acceleration of exhumation rates adjacent to the San Luis Valley as a whole (ca. 19–14 Ma; Lindsey et al., 1986b; Miggins et al., 2002; Singleton et al., 2024). The increase

in exhumation rates following the end of top-SW displacement along brittle-plastic shear zones may indicate that extension began to be accommodated along higher-angle brittle normal faults associated with the Sangre de Cristo fault system at this time. The 12.6 ± 0.6 Ma U-Pb age for apparently postkinematic hydrothermal monazite in sample 22-5-SC578 from the Deadman Creek shear zone suggests that fluid flow associated with the Sangre de Cristo fault system was locally active at least ~1 km from the range front.

Whether late Oligocene to Early Miocene Rio Grande rift extension was accommodated by similar but now obscured reactivated brittle-plastic shear zones in other parts of the range is unclear. Miocene low-angle normal faults have been documented in central New Mexico, where they locally reactivate mylonitic Proterozoic shear zones (Ricketts et al., 2015). Rift extension along an apparent chlorite-rich, low-angle normal fault ~80 km to the south of the range (at the San Luis gold mine; Benson and Jones, 1996; Benson, 1997), and chlorite-rich breccia intervals in exploratory boreholes in the San Luis Valley along a structure interpreted by Hoey et al. (2006) as a low-angle, Miocene extensional fault, provide limited evidence of more widespread extension along structures similar to the brittle-plastic shear zones found in the study area. However, evidence of low-angle extension from Hoey et al. (2006) and Watkins (1996) is broadly inconsistent with the interpreted subsurface geometry of the Sangre de Cristo fault system established in other studies (Kluth and Schaftenaar, 1994; Grauch et al., 2013; Drenth et al., 2013; Lindsey and Caine, 2024). An apparent increase in the spatial density of brittle-plastic shear zones approaching the strand of the Sangre de Cristo fault along the range front and the subparallel strike of the Sangre de Cristo fault system relative to these shear zones (Fig. 2, File S1) suggests the possibility of structural inheritance. Range-bounding normal faults in most parts of the Rio Grande rift are consistently moderate to high angle, but extension accommodated by low-angle normal faults, some of which reactivated older structures, cannot be ruled out during the earlier stages of rifting.

7.2 Extensional Shear Zone Rheology and Controls on Reactivation

A comparison between kinematics interpreted from oriented mylonite samples and the corresponding local shear zone margin dips suggests that top-SW normal-sense shear occurred in both optimally oriented zones (~60°) for an Andersonian normal fault regime and low-angle zones (<40°) misoriented in this regime (Fig. 10D). Reactivation appears to be more pervasive in the former class of shear zones, but there are several examples of extensional shear in zones dipping ~25°–40° (Fig. 10D). All shear zones that record exclusively top-NE shear dip <38°. Given the evidence of mineralizing fluid flow along range-bounding faults coeval with the early stages of Rio Grande rifting (e.g., Benson and Jones, 1996) and that the IMSZ and other mylonitic shear zones in the field area are rich in phyllosilicates, both high fluid pressure (ρ_f) and low coefficients of friction (μ) are viable candidates for enabling the reactivation of the misoriented shear zones. Besides ρ_f, other processes related to fluid migration (e.g., hydrolytic and reaction weakening) should be considered as well.

Secondary phyllosilicates (chlorite, white mica, or both) are common constituents of brittle-plastic shear zone samples. The relative proportions of these two different phyllosilicates relate to host rock mineralogy. Shear zones cutting quartzofeldspathic gneiss commonly contain more white mica, and shear zones bounded on one or both sides by amphibole-rich host rock (e.g., amphibolite-rich gneiss in the case of the entire IMSZ, and gabbro in the case of the shear zone shown in Fig. 6) tend to be richer in chlorite. The reaction-weakening process by which white mica is generated in a shear zone is locally well preserved in several samples dominated by top-NE kinematic indicators. Fractured feldspar was likely altered to white mica by hydrothermal fluids channelized along brittle fractures (e.g., Fig. 7C), and mica in turn promoted further shear and fluid flow along shear bands. Chlorite likely replaced host rock–derived hornblende through a similar process, although that process appears to have progressed more rapidly, as incipient alteration of hornblende to chlorite is very rare in mylonitic samples.

Alteration of feldspar to white mica and hornblende to chlorite is locally pervasive in samples that record dominantly or exclusively top-NE reverse-sense shear, which indicates that fluid-driven reaction softening associated with the development of secondary phyllosilicates was an important process during the earlier (presumably Laramide) contractional deformation. The chlorite-rich mylonitic fabric derived from the late Oligocene gabbro stock indicates that, at least locally, reaction softening was important during the extensional phase of deformation as well. These top-SW fabrics may have developed in the presence of hydrothermal fluid sourced from the gabbroic stock itself; from proximal, cogenetic magmatic bodies; and/or from ambient pore fluid (Fig. 14B). Small intrusive dikes and stocks are common in the study area (Fig. 2), and hydrothermal mineralization along rift-related structures is evidenced by syn-late kinematic calcite and Fe-oxide veins within our shear zone samples and by a broad zone of mostly subeconomic mineral deposits along the Sangre de Cristo fault system (Johnson et al., 1984). Localized late Oligocene heating from hydrothermal fluids and/or magmatically elevated geothermal gradients may explain how top-SW extensional shear likely occurred at temperatures of ≥300 °C and at least locally at temperatures of ~440 ± 50 °C, based on the c-axis opening angle of sample 20-9-SC34 (Fig. 11D), whereas crystalline rocks farther north locally cooled below ~250 °C prior to mid-Cenozoic extension, based on thermochronologic data (Lindsey et al., 1986b; Ghamedi et al., 2023).

Petrographic analysis indicates that top-SW fabrics formed in zones dominantly composed of phyllosilicate or along phyllosilicate-lined structures surrounded by stronger minerals, sometimes with brittle fracturing of plastically deformed quartz. Compiled estimates of microscale kinematics and modal phyllosilicate (chlorite and white mica) proportions suggest that samples preserving exclusively top-NE kinematic indicators are disproportionately phyllosilicate-poor, whereas samples with pervasive overprinting by top-SW kinematic indicators are generally richer in phyllosilicates (Fig. 10C). In petrographic sections containing mixtures of top-NE and top-SW kinematic

indicators, top-SW fabrics are more commonly localized and concentrated in intervals where phyllosilicates form the interconnected weak phase. The preservation of top-NE quartz crystallographic fabrics in IMSZ samples that pervasively (19-7-14) or locally (5-21-SC34c) record top-SW kinematic indicators (Figs. 11A and 11B) suggests that top-SW quartz dislocation creep was relatively limited compared to mylonitization during top-NE shear. Extensional deformation was consequently likely accommodated in phyllosilicate domains through dislocation glide and frictional sliding on basal planes, with the presence of interconnected phyllosilicates partially controlling whether shear zones were reactivated or not.

Most (~86%) of the shear zones identified in the study area preserve some evidence of top-SW reactivation (Figs. 10A and 10B). Reactivation appears to have been pervasive in some shear zones (e.g., with top-SW fabrics observed in almost every outcrop of the IMSZ), but in others may have been localized in thinner, mostly phyllosilicate-rich intervals. In addition to phyllosilicate content, reactivation was also likely influenced by geometry, with moderate- to higher-angle shear zones more likely to have been reactivated in extension (Fig. 10D). The Crestone thrust, which dips ~30°SW at its southern end in the study area and is apparently not reactivated, lacks mylonitic fabrics, but Pennsylvanian strata in the footwall are locally rich in fine-grained micas and dip moderate to steeply SW. The lack of normal-sense shear of these heterogeneous sedimentary units may indicate that they generally were not weak enough or continuous enough to accommodate reactivation.

8. CONCLUSIONS

Along the western flank of the Sangre de Cristo Range near Crestone, Colorado, SW-dipping brittle-plastic shear zones show extensive microstructural and macrostructural evidence for extensional (top-SW) overprinting of originally reverse-sense (top-NE), brittle-plastic deformational fabrics. Based on geometries and kinematics, these shear zones are likely of Laramide origin, whereas normal-sense overprinting is associated with the early stages of extension in the Rio Grande rift. Microstructural observations suggest that these shear zones may have originated as cataclastic fault zones during early Laramide deformation. Evolution from cataclastic zones to mylonitic fabrics characterized by quartz dislocation creep and dynamic recrystallization may relate to progressive heating from thrust burial, hydrolytic weakening, and/or a shift to lower strain rates during contractional deformation. During reverse-sense shear, reaction weakening through alteration of comminuted host-rock feldspar and hornblende produced domains rich in phyllosilicates (white mica and chlorite). Brittle fracturing of plastic fabrics, consistent with top-NE Laramide kinematics, suggests that some of the shear zones ceased to deform plastically while still accommodating Laramide shortening.

Extensional, top-SW reactivation is constrained to the latest Oligocene–earliest Miocene by a 25.6 ± 0.7 Ma zircon U-Pb date for a gabbro stock cut by one of the top-SW shear zones. A zircon fission-track date of 26.7 + 3.6/–3.2 Ma from the gabbroic stock indicates that shearing was locally short lived and may have occurred during magmatic cooling. U-Th-Pb dates from late synkinematic monazite constrain the end of extensional displacement along the reactivated shear zones to the late Oligocene to Early Miocene (≥21 Ma). Extensional fabrics are characterized by S-C-C′ fabrics in phyllosilicate-rich domains, with C′ shear bands locally fracturing quartz that was previously plastically deformed during contractional shearing. Top-SW deformation was accommodated primarily through dislocation glide and frictional sliding along basal planes in phyllosilicate, locally in addition to quartz dislocation creep and brittle fracturing. Extensional overprinting is concentrated in more steeply dipping shear zone domains and where phyllosilicates form an interconnected weak phase, with contractional fabrics better preserved in more shallowly dipping domains and where quartz or feldspar forms the dominant interconnected phase. Reactivation was thus governed by geometry and shear zone rheology significantly affected by fluid-related reaction weakening during the contractional phase of deformation.

The apparent end of extensional displacement along the reactivated shear zones predated or roughly coincided with an increase in local extension rates. Extensional strain likely shifted to the subparallel, range-bounding Sangre de Cristo fault system at this time. Reactivation of weak, nonoptimally oriented Laramide structures may have been a widespread process by which midcrustal extension was accommodated during the earliest stages of Rio Grande rifting.

ACKNOWLEDGMENTS

This research was funded by National Science Foundation award 2115719 and the U.S. Geological Survey (USGS) EDMAP Program award G21AC10493. J.S. Caine acknowledges support from the USGS Mineral Resources Program. Any use of trade, firm, or product names is for descriptive purposes only and does not imply endorsement by the U.S. Government. We thank David Lindsey (USGS Emeritus), Katrina Sauer (USGS), and Kevin Jones (USGS), as well as Geosphere reviewers Jason Ricketts and Michael Wells, for their very helpful comments on this manuscript. This research was built on David Lindsey's pioneering work in the Sangre de Cristo Range. We also thank Paula Leek for making numerous high-quality thin sections for this project.

REFERENCES CITED

Abbey, A.L., and Niemi, N.A., 2020, Perspectives on continental rifting processes from spatiotemporal patterns of faulting and magmatism in the Rio Grande Rift, USA: Tectonics, v. 39, no. 1, https://doi.org/10.1029/2019TC005635.

Allmendinger, R.W., Cardozo, N., and Fisher, D.M., 2013, Structural Geology Algorithms: Vectors and Tensors: Cambridge, UK, Cambridge University Press, 302 p.

Anderson, E.M., 1905, The dynamics of faulting: Transactions of the Edinburgh Geological Society, v. 8, no. 3, p. 387–402, https://doi.org/10.1144/transed.8.3.387.

Behr, W.M., and Platt, J.P., 2014, Brittle faults are weak, yet the ductile middle crust is strong: Implications for lithospheric mechanics: Geophysical Research Letters, v. 41, no. 22, p. 8067–8075, https://doi.org/10.1002/2014GL061349.

Benson, R.G., 1997, Detachment fault-related mineralization in a rift setting at the San Luis gold deposit and Sangre de Cristo Mountains, Alamosa, Costilla, and Saguache counties, Colorado [Ph.D. dissertation]: Golden, Colorado, USA, Colorado School of Mines, 226 p.

Benson, R.G., and Jones, D.M., 1996, Geology of the San Luis Gold Deposit, Costilla County, Colorado: An Example of Low-Angle Normal Fault and Rift-Related Mineralization in the Sangre de Cristo Range of Colorado: Golden, Colorado, USA, Colorado School of Mines, https://berthoud.catalog.aspencat.info/ColoGovDoc/on1061561798.

Blakey, R.C., and Ranney, W.D., 2018, Ancient Landscapes of Western North America: A Geologic History with Paleogeographic Maps: New York, Springer, 228 p, https://doi.org/10.1007/978-3-319-59636-5.

Bos, B., and Spiers, C.J., 2002, Frictional-viscous flow of phyllosilicate-bearing fault rock: Microphysical model and implications for crustal strength profiles: Journal of Geophysical Research: Solid Earth, v. 107, no. B2.

Brister, B.S., and Gries, R.R., 1994, Tertiary stratigraphy and tectonic development of the Alamosa basin (northern San Luis Basin), Rio Grande rift, South-Central Colorado, *in* Keller, G.R., and Cather, S.M., eds., Basins of the Rio Grande Rift: Structure, Stratigraphy, and Tectonic Setting: Geological Society of America Special Paper 291, p. 39–58, https://doi.org/10.1130/SPE291-p39.

Bush, M.A., Horton, B.K., Murphy, M.A., and Stockli, D.F., 2016, Detrital record of initial basement exhumation along the Laramide deformation front, southern Rocky Mountains: Tectonics, v. 35, no. 9, p. 2117–2130, https://doi.org/10.1002/2016TC004194.

Byerlee, J., 1978, Friction of rocks: Pure and Applied Geophysics, v. 116, no. 4–5, p. 615–626, https://doi.org/10.1007/BF00876528.

Caine, J.S., Grauch, V.J.S., and Lindsey, D.A., 2013, Tales of the Deadman Thrust: Northeast verging folds, injection breccias, and high-angle normal faults in the rift-flanking basement of the Sangre de Cristo mountains, Colorado: Geological Society of America Abstracts with Programs, v. 45, no. 7, p. 443.

Caine, J.S., Minor, S.A., Grauch, V.J.S., Budahn, J.R., and Keren, T.T., 2017, A comprehensive survey of faults, breccias, and fractures in and flanking the eastern Española Basin, Rio Grande rift, New Mexico: Geosphere, v. 13, p. 1566–1609, https://doi.org/10.1130/GES01348.1.

Carpenter, B.M., Saffer, D.M., and Marone, C., 2012, Frictional properties and sliding stability of the San Andreas fault from deep drill core: Geology, v. 40, p. 759–762, https://doi.org/10.1130/G33007.1.

Cather, S., 2004, Laramide orogeny in central and northern New Mexico and southern Colorado, *in* Mack, G.H., and Giles, K.A., eds., The Geology of New Mexico: A Geologic History: New Mexico Geological Society Special Publication 11, p. 203–248.

Clement, J.F., 1952, The geology of the northeastern Baca Grant area, Saguache County, Colorado [M.S. thesis]: Golden, Colorado, USA, Colorado School of Mines, 129 p.

Collettini, C., 2011, The mechanical paradox of low-angle normal faults: Current understanding and open questions: Tectonophysics, v. 510, no. 3–4, p. 253–268, https://doi.org/10.1016/j.tecto.2011.07.015.

Collettini, C., Tesei, T., Scuderi, M.M., Carpenter, B.M., and Viti, C., 2019, Beyond Byerlee friction, weak faults and implications for slip behavior: Earth and Planetary Science Letters, v. 519, p. 245–263, https://doi.org/10.1016/j.epsl.2019.05.011.

Drenth, B.J., Grauch, V.J., and Rodriguez, B.D., 2013, Geophysical constraints on Rio Grande rift structure in the central San Luis Basin, Colorado and New Mexico, *in* Hudson, M.R., and Grauch, W.J.S., New Perspectives on Rio Grande Rift Basins: From Tectonics to Groundwater: Geological Society of America Special Paper 494, p. 75–99, https://doi.org/10.1130/2013.2494(04).

Faleiros, F.M., Moraes, R.D., Pavan, M., and Campanha, G.A.D.C., 2016, A new empirical calibration of the quartz c-axis fabric opening-angle deformation thermometer: Tectonophysics, v. 671, p. 173–182, https://doi.org/10.1016/j.tecto.2016.01.014.

Fletcher, J.M., Coogan, J., Benson, C.W., Csar, A.J., Gullet, C.J., Oliver, S.R., and Teran, O.J., 2006, Role of tectonic inheritance and mode of continental extension in the Upper Rio Grande Rift: Geological Society of America Abstracts with Programs, v. 38, no. 6, p. 37, https://gsa.confex.com/gsa/2006RM/webprogram/Paper104884.html.

Ghamedi, O., Singleton, J., Sitar, M.C., Rahl, J., Wong, M., O'Sullivan, P., Hurtado, C., and Malavarca, S., 2023, Refining the pre- and syn-Rio Grande rift cooling history across the Sangre de Cristo Range and Alvarado fault through application of mid- to low-temperature thermochronometry: Geological Society of America Abstracts with Programs, v. 55, no. 5, https://doi.org/10.1130/abs/2023RM-387970.

Grauch, V.J., Bedrosian, P.A., and Drenth, B.J., 2013, Advancements in understanding the aeromagnetic expressions of basin-margin faults—An example from San Luis Basin, Colorado: The Leading Edge, v. 32, no. 8, p. 882–891, https://doi.org/10.1190/tle32080882.1.

Griggs, D., 1967, Hydrolytic weakening of quartz and other silicates*: Geophysical Journal International, v. 14, no. 1–4, p. 19–31, https://doi.org/10.1111/j.1365-246X.1967.tb06218.x.

Handy, M.R., 1990, The solid-state flow of polymineralic rocks: Journal of Geophysical Research: Solid Earth, v. 95, p. 8647–8661, https://doi.org/10.1029/JB095iB06p08647.

Hoey, N., Watkins, T.A., and Parsons, K., 2006, A summary review including a work plan and budget proposal to test oil and gas prospects on the San Luis basin property, Colorado, USA: Lexam Explorations, Inc., Watts, Griffis and McOuat Limited.

Holm-Denoma, C.S., Caine, J.S., and Pianowski, L.S., 2019, U-Pb zircon data for: The Poncha Pass and Deadman Creek areas, northern Sangre de Cristo Mountains of south-central Colorado: U.S. Geological Survey data release, https://doi.org/10.5066/P96HNSNL.

Hoy, R.G., and Ridgway, K.D., 2002, Syndepositional thrust-related deformation and sedimentation in an Ancestral Rocky Mountains basin, Central Colorado trough, Colorado, USA: Geological Society of America Bulletin, v. 114, p. 804–828, https://doi.org/10.1130/0016-7606(2002)114<0804:STRDAS>2.0.CO;2.

Janots, E., Berger, A., Gnos, E., Whitehouse, M., Lewin, E., and Pettke, T., 2012, Constraints on fluid evolution during metamorphism from U–Th–Pb systematics in Alpine hydrothermal monazite: Chemical Geology, v. 326–327, p. 61–71, https://doi.org/10.1016/j.chemgeo.2012.07.014.

Johnson, B.R., Lindsey, D.A., Ellis, C.E., Hannigan, B.J., and Thompson, J.R., 1984, Mineral resource potential of the Sangre de Cristo Wilderness study area, south-central Colorado: U.S. Geological Survey Miscellaneous Field Studies Map 1635-A, https://doi.org/10.3133/mf1635A.

Johnson, B.R., Lindsey, D.A., Bruce, R.M., and Soulliere, S.J., 1987, Reconnaissance geologic map of the Sangre de Cristo Wilderness study area, south-central Colorado: U.S. Geological Survey Miscellaneous Field Studies Map 1635-B, https://doi.org/10.3133/mf1635B.

Johnson, R.B., 1969, Geologic map of the Trinidad quadrangle, south-central Colorado: U.S. Geological Survey Miscellaneous Geologic Investigations Map I-558, scale 1:250,000.

Jones, J.V., III, and Connelly, J.N., 2006, Proterozoic tectonic evolution of the Sangre de Cristo Mountains, southern Colorado, U.S.A: Rocky Mountain Geology, v. 41, no. 2, p. 79–116, https://doi.org/10.2113/gsrocky.41.2.79.

Kelley, S.A., Chapin, C.E., and Corrigan, J., 1992, Late Mesozoic to Cenozoic cooling histories of the flanks of the northern and central Rio Grande rift, Colorado and New Mexico: New Mexico Institute of Mining & Technology Bulletin 145, https://doi.org/10.58799/B-145.

Kluth, C.F., and Schaftenaar, C.H., 1994, Depth and geometry of the northern Rio Grande rift in the San Luis Basin, south-central Colorado, *in* Keller, G.R., and Cather, S.M., eds., Basins of the Rio Grande Rift: Structure, Stratigraphy, and Tectonic Setting: Geological Society of America Special Paper 291, https://doi.org/10.1130/SPE291-p27.

Kohlstedt, D.L., Evans, B., and Mackwell, S.J., 1995, Strength of the lithosphere: Constraints imposed by laboratory experiments: Journal of Geophysical Research: Solid Earth, v. 100, no. B9, p. 17,587–17,602, https://doi.org/10.1029/95JB01460.

Kylander-Clark, A.R., Hacker, B.R., and Cottle, J.M., 2013, Laser-ablation split-stream ICP petrochronology: Chemical Geology, v. 345, p. 99–112, https://doi.org/10.1016/j.chemgeo.2013.02.019.

Lindsey, D.A., 1998, Laramide structure of the central Sangre de Cristo Mountains and adjacent Raton basin, southern Colorado: The Mountain Geologist, v. 35, no. 2, p. 55–70.

Lindsey, D.A., 2010, The geologic story of Colorado's Sangre de Cristo Range: U.S. Geological Survey Circular 1349, p. 1–18, https://doi.org/10.3133/cir1349.

Lindsey, D.A., and Caine, J.S., 2024, Thick- and thin-skinned contractional styles and the tectonic evolution of the northern Sangre de Cristo Mountains, Colorado, USA: Geosphere, v. 20, p. 678–710, https://doi.org/10.1130/GES02635.1.

Lindsey, D.A., Johnson, B.R., and Andriessen, P.A.M., 1983, Laramide and Neogene structure of the northern Sangre de Cristo Range, south-central Colorado, *in* Lowell, J.A., ed., Rocky Mountain Foreland Basins and Uplifts: Denver, Colorado, USA, Rocky Mountain Association of Geologists, p. 219–228.

Lindsey, D.A., Soulliere, S.J., Hafner, K., and Flores, R.J., 1985, Geologic map of Rito Alto Peak and northeastern part of Mirage quadrangles, Custer and Saguache counties, Colorado: U.S. Geological Survey Miscellaneous Field Studies Map 1787, https://doi.org/10.3133/mf1787

Lindsey, D.A., Johnson, B.R., Soulliere, S.J., Bruce, R.M., and Hafner, K., 1986a, Geologic map of the Beck Mountain, Crestone Peak, and Crestone quadrangles, Custer, Huerfano, and Saguache counties, Colorado: U.S. Geological Survey Miscellaneous Field Studies Map 1878, https://doi.org/10.3133/mf1878.

Lindsey, D.A., Andriessen, P.M., and Wardlaw, B.R., 1986b, Heating, cooling, and uplift during Tertiary time, northern Sangre de Cristo Range, Colorado: Geological Society of America Bulletin, v. 97, p. 1133–1143, https://doi.org/10.1130/0016-7606(1986)97<1133:HCAUDT>2.0.CO;2.

Lindsey, D.A., Clark, R.F., and Soulliere, S.J., 1986c, Minturn and Sangre de Cristo formations of southern Colorado: A prograding fan delta and alluvial fan sequence shed from the Ancestral Rocky Mountains, *in* Peterson, J.A., ed., Paleotectonics and Sedimentation in the Rocky

Mountain Region, United States: American Association of Petroleum Geologists Memoir 41, p. 541–561, https://doi.org/10.1306/M41456C26.
Lipman, P.W., 1975, Evolution of the Platoro caldera complex and related volcanic rocks, southeastern San Juan Mountains, Colorado: U.S. Geological Survey Professional Paper 852, 128 p., https://doi.org/10.3133/pp852.
Lipman, P.W., and McIntosh, W.C., 2011, Tertiary Volcanism in the Eastern San Juan Mountains. The Eastern San Juan Mountains: Their Geology, Ecology, and Human History: Denver, Colorado, USA, University Press of Colorado, p. 17–37.
Lipman, P.W., Steven, T.A., and Mehnert, H.H., 1970, Volcanic history of the San Juan Mountains, Colorado, as indicated by potassium–argon dating: Geological Society of America Bulletin, v. 81, p. 2329–2352, https://doi.org/10.1130/0016-7606(1970)81[2329:VHOTSJ]2.0.CO;2.
Lisenbee, A.L., 2013, Multi-stage Laramide deformation in the area of the Southern Santa Fe embayment (Rio Grande rift), north-central New Mexico, *in* Hudson, M.R., and Grauch, V.J.S., eds., New Perspectives on Rio Grande Rift Basins: From Tectonics to Groundwater: Geological Society of America Special Paper 494, https://doi.org/10.1130/2013.2494(10).
Malavarca, S., Singleton, J., Sitar, M., Rahl, J., and Magloughlin, J.F., 2023, Cenozoic metamorphism and along-strike peak temperatures in the Pennsylvanian Minturn Formation in the Sangre de Cristo Range: Unravelling the complex thermal history of the Rio Grande rift in southern Colorado: Geological Society of America Abstracts with Programs, v. 55, no. 5, https://doi.org/10.1130/abs/2023RM-387928.
McCalpin, J., 1981, Quaternary geology and neotectonics of the west flank of the northern Sangre de Cristo Mountains, south-central Colorado [Ph.D. thesis]: Golden, Colorado, USA, Colorado School of Mines, https://doi.org/10.13140/RG.2.2.25742.77129.
McIntosh, W.C., and Chapin, C.E., 2004, Geochronology of the central Colorado volcanic field, *in* Cather, S.M., McIntosh, W.C., and Kelley, S.A., eds., Tectonics, geochronology, and volcanism in the Southern Rocky Mountains and Rio Grande rift: New Mexico Bureau of Geology & Mineral Resources Bulletin 160.
Miggins, D.P., Thompson, R.A., Pillmore, C.L., Snee, L.W., and Stern, C.R., 2002, Extension and uplift of the northern Rio Grande Rift: Evidence from $^{40}Ar/^{39}Ar$ geochronology from the Sangre de Cristo Mountains, south-central Colorado and northern New Mexico, *in* Menzier, M.A., Klemperer, S.L., Ebinger, C.J., and Baker, J., eds., Volcanic Rifted Margins: Geological Society of America Special Paper 362, https://doi.org/10.1130/0-8137-2362-0.47.
Neumann, B., 2000, Texture development of recrystallised quartz polycrystals unravelled by orientation and misorientation characteristics: Journal of Structural Geology, v. 22, p. 1695–1711, https://doi.org/10.1016/S0191-8141(00)00060-2.
O'Hara, K., 1988, Fluid flow and volume loss during mylonitization: An origin for phyllonite in an overthrust setting, North Carolina U.S.A: Tectonophysics, v. 156, no. 1–2, p. 21–36, https://doi.org/10.1016/0040-1951(88)90280-6.
Passchier, C.W., and Trouw, R.A., 2005, Microtectonics (2nd edition): Berlin, Springer, 366 p.
Paton, C., Hellstrom, J., Paul, B., Woodhead, J., and Hergt, J., 2011, Iolite: Freeware for the visualisation and processing of mass spectrometric data: Journal of Analytical Atomic Spectrometry, v. 26, no. 12, p. 2508–2518, https://doi.org/10.1039/c1ja10172b.
Reiners, P.W., and Brandon, M.T., 2006, Using thermochronology to understand orogenic erosion: Annual Review of Earth and Planetary Sciences, v. 34, no. 1, p. 419–466, https://doi.org/10.1146/annurev.earth.34.031405.125202.
Ricketts, J.W., Karlstrom, K.E., and Kelley, S.A., 2015, Embryonic core complexes in narrow continental rifts: The importance of low-angle normal faults in the Rio Grande rift of central New Mexico: Geosphere, v. 11, p. 425–444, https://doi.org/10.1130/GES01109.1.
Ricketts, J.W., Kelley, S.A., Karlstrom, K.E., Schmandt, B., Donahue, M.S., and van Wijk, J., 2016, Synchronous opening of the Rio Grande Rift along its entire length at 25–10 Ma supported by apatite (U-Th)/He and fission-track thermochronology, and evaluation of possible driving mechanisms: Geological Society of America Bulletin, v. 128, p. 397–424, https://doi.org/10.1130/B31223.1.
Ruleman, C.A., and Brandt, T.R., 2021, Surficial geology of the northern San Luis Valley, Saguache, Fremont, Custer, Alamosa, Rio Grande, Conejos, and Costilla counties, Colorado: U.S. Geological Survey Scientific Investigations Map 3475, https://doi.org/10.3133/sim3475
Sibson, R.H., 1983, Continental fault structure and the shallow earthquake source: Journal of the Geological Society, v. 140, no. 5, p. 741–767, https://doi.org/10.1144/gsjgs.140.5.0741.
Sibson, R.H., 1985, A note on fault reactivation: Journal of Structural Geology, v. 7, no. 6, p. 751–754, https://doi.org/10.1016/0191-8141(85)90150-6.
Singleton, J., Ghamedi, O., Malavarca, S., Sitar, M., Wong, M., Rahl, J., and O'Sullivan, P., 2024, New insights into Laramide contraction, Oligocene metamorphism, and Rio Grande rift extension in the Sangre de Cristo Range (southern Colorado) from mid- and low-temperature thermochronology: Geological Society of America Abstracts with Programs, v. 56, no. 5, https://doi.org/10.1130/abs/2024AM-402844.
Sitar, M.C., 2023, Geologic mapping and kinematic analysis of the Independence Mine shear zone in the Sangre de Cristo Range, southern Colorado: Extensional reactivation of a Laramide reverse fault [M.S. thesis]: Fort Collins, Colorado, USA, Colorado State University, 128 p.
Smith, T.M., Saylor, J.E., Lapen, T.J., Hatfield, K., and Sundell, K.E., 2023, Identifying sources of non-unique detrital age distributions through integrated provenance analysis: An example from the Paleozoic Central Colorado Trough: Geosphere, v. 19, p. 471–492, https://doi.org/10.1130/GES02541.1.
Steven, T.A., and Lipman, P.W., 1975, Calderas of the San Juan volcanic field, southwestern Colorado: U.S. Geological Survey Professional Paper 958, https://doi.org/10.3133/pp958
Sweet, D.E., and Soreghan, G.S., 2010, Late Paleozoic tectonics and paleogeography of the ancestral Front Range: Structural, stratigraphic, and sedimentologic evidence from the Fountain Formation (Manitou Springs, Colorado): Geological Society of America Bulletin, v. 122, p. 575–594, https://doi.org/10.1130/B26554.1.
Sweet, D.E., Brotherton, J.L., Chowdhury, N.U.M.K., and Ramsey, C.E., 2021, Tectonic subsidence analysis of the Ancestral Rocky Mountains from the interior to the southern margin: Palaeogeography, Palaeoclimatology, Palaeoecology, v. 576, https://doi.org/10.1016/j.palaeo.2021.110508.
Thacker, J.O., Karlstrom, K.E., Kelley, S.A., Crow, R.S., and Kendall, J.J., 2023, Late Cretaceous time-transgressive onset of Laramide arch exhumation and basin subsidence across northern Arizona–New Mexico, USA, and the role of a dehydrating Farallon flat slab: Geological Society of America Bulletin, v. 135, p. 389–406, https://doi.org/10.1130/B36245.1.
Tweto, O., 1975, Laramide (Late Cretaceous-early Tertiary) orogeny in the Southern Rocky Mountains, *in* Curtis, Bruce F., ed., Cenozoic History of the Southern Rocky Mountains: Geological Society of America Memoir 144, https://doi.org/10.1130/MEM144-p1.
Vermeesch, P., 2018, IsoplotR: A free and open toolbox for geochronology: Geoscience Frontiers, v. 9, p. 1479–1493, https://doi.org/10.1016/j.gsf.2018.04.001.
Wallace, A.R., 2004, Evolution of the southeastern San Luis Basin margin and the Culebra embayment, Rio Grande rift, southern Colorado, *in* Geology of the Taos Region: New Mexico Geological Society, 55th Field Conference Guidebook, p. 181–192, https://doi.org/10.56577/FFC-55.181.
Wallis, D., Lloyd, G.E., Phillips, R.J., Parsons, A.J., and Walshaw, R.D., 2015, Low effective fault strength due to frictional-viscous flow in phyllonites, Karakoram Fault Zone, NW India: Journal of Structural Geology, v. 77, p. 45–61, https://doi.org/10.1016/j.jsg.2015.05.010.
Watkins, T.A., 1996, Geology of the northeastern San Luis Basin, Saguache County, Colorado: Geological Society of America Field Trip Guidebook for the 1996 Annual Meeting.
Weigel, J.F., 2014, Evaluation of thrusting and folding of the Deadman Creek thrust fault, Sangre de Cristo Range, Saguache County, Colorado [M.Sc. thesis]: Golden, Colorado, USA, Colorado School of Mines, https://repository.mines.edu/handle/11124/12279.
Yonkee, W.A., Parry, W.T., and Bruhn, R.L., 2003, Relations between progressive deformation and fluid-rock interaction during shear-zone growth in a basement-cored thrust sheet, Sevier orogenic belt, Utah: American Journal of Science, v. 303, no. 1, p. 1–59, https://doi.org/10.2475/ajs.303.1.1.